



**HAL**  
open science

# Constraints on melt content of off-axis magma lenses at the East Pacific Rise from analysis of 3-D seismic amplitude variation with angle of incidence

Omid Aghaei, Mladen R. Nedimović, Milena Marjanović, Suzanne M. Carbotte, J. Pablo Canales, Hélène Carton, Nikola Nikić

## ► To cite this version:

Omid Aghaei, Mladen R. Nedimović, Milena Marjanović, Suzanne M. Carbotte, J. Pablo Canales, et al.. Constraints on melt content of off-axis magma lenses at the East Pacific Rise from analysis of 3-D seismic amplitude variation with angle of incidence. *Journal of Geophysical Research: Solid Earth*, 2017, 122, pp.4123-4142. 10.1002/2016JB013785 . insu-03748854

**HAL Id: insu-03748854**

**<https://insu.hal.science/insu-03748854>**

Submitted on 10 Aug 2022

**HAL** is a multi-disciplinary open access archive for the deposit and dissemination of scientific research documents, whether they are published or not. The documents may come from teaching and research institutions in France or abroad, or from public or private research centers.

L'archive ouverte pluridisciplinaire **HAL**, est destinée au dépôt et à la diffusion de documents scientifiques de niveau recherche, publiés ou non, émanant des établissements d'enseignement et de recherche français ou étrangers, des laboratoires publics ou privés.

Copyright

## RESEARCH ARTICLE

10.1002/2016JB013785

## Key Points:

- Investigated midcrustal off-axis magma lenses are partially molten and contain a smaller amount of melt than the axial magma lens
- Melt-poor state of studied off-axis magma lenses is largely the result of limited melt supply from the underlying mantle source reservoir
- Studied off-axis magma lenses have a longer period of melt replenishment and lower eruption recurrence rates than the axial magma lens

## Correspondence to:

M. R. Nedimović,  
mladen@dal.ca

## Citation:

Aghaei, O., M. R. Nedimović, M. Marjanović, S. M. Carbotte, J. Pablo Canales, H. Carton, and N. Nikić (2017), Constraints on melt content of off-axis magma lenses at the East Pacific Rise from analysis of 3-D seismic amplitude variation with angle of incidence, *J. Geophys. Res. Solid Earth*, 122, 4123–4142, doi:10.1002/2016JB013785.

Received 22 NOV 2016

Accepted 18 MAY 2017

Accepted article online 22 MAY 2017

Published online 28 JUN 2017

## Constraints on melt content of off-axis magma lenses at the East Pacific Rise from analysis of 3-D seismic amplitude variation with angle of incidence

Omid Aghaei<sup>1,2</sup>, Mladen R. Nedimović<sup>1,3</sup>, Milena Marjanović<sup>4</sup>, Suzanne M. Carbotte<sup>3</sup>, J. Pablo Canales<sup>5</sup>, Hélène Carton<sup>3,4</sup> , and Nikola Nikić<sup>6,7</sup>

<sup>1</sup>Department of Earth Sciences, Dalhousie University, Halifax, Nova Scotia, Canada, <sup>2</sup>Now at Shell Canada Energy, Calgary, Alberta, Canada, <sup>3</sup>Lamont-Doherty Earth Observatory, Columbia University, Palisades, New York, USA, <sup>4</sup>Institut de Physique du Globe de Paris, Paris, France, <sup>5</sup>Woods Hole Oceanographic Institution, Woods Hole, Massachusetts, USA, <sup>6</sup>Paradigm Geophysical Ltd, Houston, Texas, USA, <sup>7</sup>Now at Absolute Imaging Inc., Calgary, Alberta, Canada

**Abstract** We use 3-D multichannel seismic data to form partial angle  $P$  wave stacks and apply amplitude variation with angle (AVA) crossplotting to assess melt content and melt distribution within two large midcrustal off-axis magma lenses (OAMLs) found along the East Pacific Rise from 9°37.5'N to 9°57'N. The signal envelope of the partial angle stacks suggests that both OAMLs are partially molten with higher average melt content and more uniform melt distribution in the southern OAML than in the northern OAML. For AVA crossplotting, the OAMLs are subdivided into seven  $\sim 1$  km<sup>2</sup> analysis windows. The AVA crossplotting results indicate that the OAMLs contain a smaller amount of melt than the axial magma lens (AML). For both OAMLs, a higher melt fraction is detected within analysis windows located close to the ridge axis than within the most distant windows. The highest average melt concentration is interpreted for the central sections of the OAMLs. The overall low OAML melt content could be indicative of melt lost due to recent off-axis eruptions, drainage to the AML, or limited mantle melt supply. Based on the results of this and earlier bathymetric, morphological, geochemical, and geophysical investigations, we propose that the melt-poor OAML state is largely the result of limited melt supply from the underlying mantle source reservoir with smaller contribution attributed to melt leakage to the AML. We hypothesize that the investigated OAMLs have a longer period of melt replenishment, lower eruption recurrence rates, and lower eruption volumes than the AML, though some could be single intrusion events.

### 1. Introduction

Crustal accretion at intermediate-to-fast spreading mid-ocean ridges is believed to occur in a narrow axial zone [e.g., Herron *et al.*, 1978; Detrick *et al.*, 1987]. This accretion zone is characterized by a thin ( $< \sim 100$  m), elongated midcrustal magma body known as the axial magma lens (AML) that sits atop of a  $\sim 5$ – $10$  km wide low-velocity zone with interstitial melt that extends to the base of the crust and uppermost mantle [e.g., Vera *et al.*, 1990; Hussenoeder *et al.*, 1996; Dunn *et al.*, 2000]. Additional vertically stacked subaxial magma lenses in the lower crust [Canales *et al.*, 2009; Marjanović *et al.*, 2014] and the Moho transition zone (MTZ) [Aghaei *et al.*, 2014] have been imaged within the axial low-velocity zone and are believed to also contribute to axial crustal accretion. However, in addition to on-axis magmatism, there is a growing body of evidence for off-axis magmatism related to magma ascent at mid-ocean ridges and therefore continuation of crustal accretion away from the narrow axial zone [e.g., Perfit *et al.*, 1994; Goldstein *et al.*, 1994; Crawford and Webb, 2002; Sims *et al.*, 2003; Nedimović *et al.*, 2005; Durant and Toomey, 2009; Canales *et al.*, 2012]. For example, Durant and Toomey [2009] attributed their observations of  $P$  wave diffractions, seismic attenuation, and  $P$ -to- $S$  wave converted phases about 20 km east of the East Pacific Rise (EPR) axis at 9°20'N to the presence of a melt lens about 2 km beneath the seafloor that is underlain by low-velocity, high attenuation crust. Results from seafloor compliance measurements at the EPR show low-velocity partial melt zones in the lower crust extending into the uppermost mantle, from  $\sim 4.5$  to  $\sim 6.5$  km below seafloor (bsf), 10 km east of the ridge axis at 9°48'N, and MTZ melt sills ( $\sim 9$  km bsf) about 2.5 km east of the ridge axis at 9°08'N [Crawford and Webb, 2002]. On the EPR ridge flanks at 9°30'–9°32'N and 9°48'–9°52'N, petrological studies identify anomalously young basalts

up to ~4 km from the ridge axis [e.g., Goldstein *et al.*, 1994; Perfit *et al.*, 1994; Sims *et al.*, 2003], suggesting off-axis volcanism.

The most direct evidence for off-axis magmatism has come from the results of a high-resolution 3-D multi-channel seismic (MCS) reflection survey conducted between 9°37.5'N and 9°57'N on the EPR that show images of a network of lower crust to midcrust reflectors at distances from 1–2 to 10–15 km away from the ridge axis [Canales *et al.*, 2012; Aghaei *et al.*, 2014; Han *et al.*, 2014]. These off-axis seismic reflectors are interpreted as magma lenses based on the reversed polarity of the reflection events relative to the seafloor and the Moho. Additional support for this interpretation comes from ocean bottom seismometer recordings that show strong attenuation of seismic waves propagating through the lower crust in the area where reflection events with reversed polarity are imaged [Canales *et al.*, 2012]. The melt content and distribution of these off-axis magma lenses (OAMLs) have not been determined, yet such constraints have the potential to shed light on the dynamics of off-axis magmatism and its relationship with on-axis magmatism [e.g., Forsyth, 1992].

The possibility of determining melt content of midcrustal axial magma bodies has been investigated at several point locations along the EPR and the Juan de Fuca Ridge by using 2-D MCS data and applying forward waveform modeling [Hussenoeder *et al.*, 1996] and waveform inversion [Collier and Singh, 1997, 1998; Singh *et al.*, 1998; Canales *et al.*, 2006; Xu *et al.*, 2014] of common midpoint gathers. The application of these methods provided a quantitative measure of the in situ melt content of the AML. Also applied in 2-D [e.g., Singh *et al.*, 1998; Canales *et al.*, 2006; Xu *et al.*, 2014] was partial offset stacking of the *P*-to-*S* converted AML reflected waves that convert back to *P* waves at the seafloor and in 3-D [Singh *et al.*, 2006] partial offset stacking of the *P*-to-*P* AML reflected waves. The *P*-*S*-*P* 2-D and *P*-*P* 3-D partial offset stacks provide qualitative estimates of along-axis variations in melt content of the AML. More recently, the applicability of the amplitude variation with angle of incidence (AVA) crossplotting technique [Castagna *et al.*, 1998] for determining spatial variations in melt content of the AML was investigated by Marjanović *et al.* [2015] using 2-D MCS data collected along the EPR from 9°29.8'N to 9°58.4'N. This study shows that AVA crossplotting can be successfully applied to a crystalline rock environment and can provide information about along-axis variations in melt content of the AML. The obtained results are in agreement with those obtained by the *P*-*S*-*P* converted phase partial offset stacking and 1-D waveform inversion applied to the same data set by Xu *et al.* [2014]. It is notable that while a single 1-D waveform inversion may still provide superior constraints on the melt content of a magma lens at any chosen point, the advantage of the AVA crossplotting approach is that it can be efficiently applied in 3-D to large sections or even the whole magma lens.

In this paper, the melt content and distribution within two large midcrustal OAMLs found along the northern EPR from 9°37.5'N to 9°57'N is assessed from partial angle *P* wave stacks and the AVA crossplotting technique applied to 3-D MCS data. The AVA crossplotting results provide an estimate of the average melt content of the OAMLs, while the *P* wave partial angle stacks provide constraints on the distribution of melt within the OAMLs. This is both the first magma reservoir melt content study targeting OAMLs and the first investigation that applies the AVA crossplotting technique to 3-D MCS data from a crystalline rock environment.

## 2. Data and Study Area

The data used in this study were collected on R/V *Marcus G. Langseth* during cruise MGL0812 in summer of 2008 across a 37 km long section of the fast-spreading EPR between 9°37.5'N and 9°57'N (Figure 1). The survey extends on both ridge flanks out to ~15 km away from the ridge axis (full fold imaging to ~12 km) or to ~180 kyr old crust assuming constant full spreading rate of 11 cm/yr for the Brunhes interval [Carbotte and Macdonald, 1992]. Two areas of 3-D coverage, separated by a 3.3 km gap, were acquired. The northern area covers ~714 km<sup>2</sup> and is located between 9°42'N and 9°57'N. The smaller, southern area covers ~100 km<sup>2</sup> and is located from 9°37.5'N to 9°40'N. Details on data acquisition are given in Mutter *et al.* [2009] and Aghaei *et al.* [2014]. The geometry of the survey yields common midpoint bins that are 37.5 m wide and 6.25 m long in along-ridge axis and cross-ridge axis directions, respectively.

The investigated portion of the EPR has experienced two well-documented volcanic eruptions in 1991–1992 [e.g., Haymon *et al.*, 1993] and 2005–2006 [e.g., Tolstoy *et al.*, 2006; Soule *et al.*, 2007] and has been the subject of numerous geologic, geomorphic, geophysical, and hydrothermal surveys making it the most comprehensively investigated section of the global mid-ocean ridge system. The axial zone of the EPR in this area is also the most densely and the most frequently sampled portion of any mid-ocean ridge [e.g., Perfit and Chadwick, 1998;

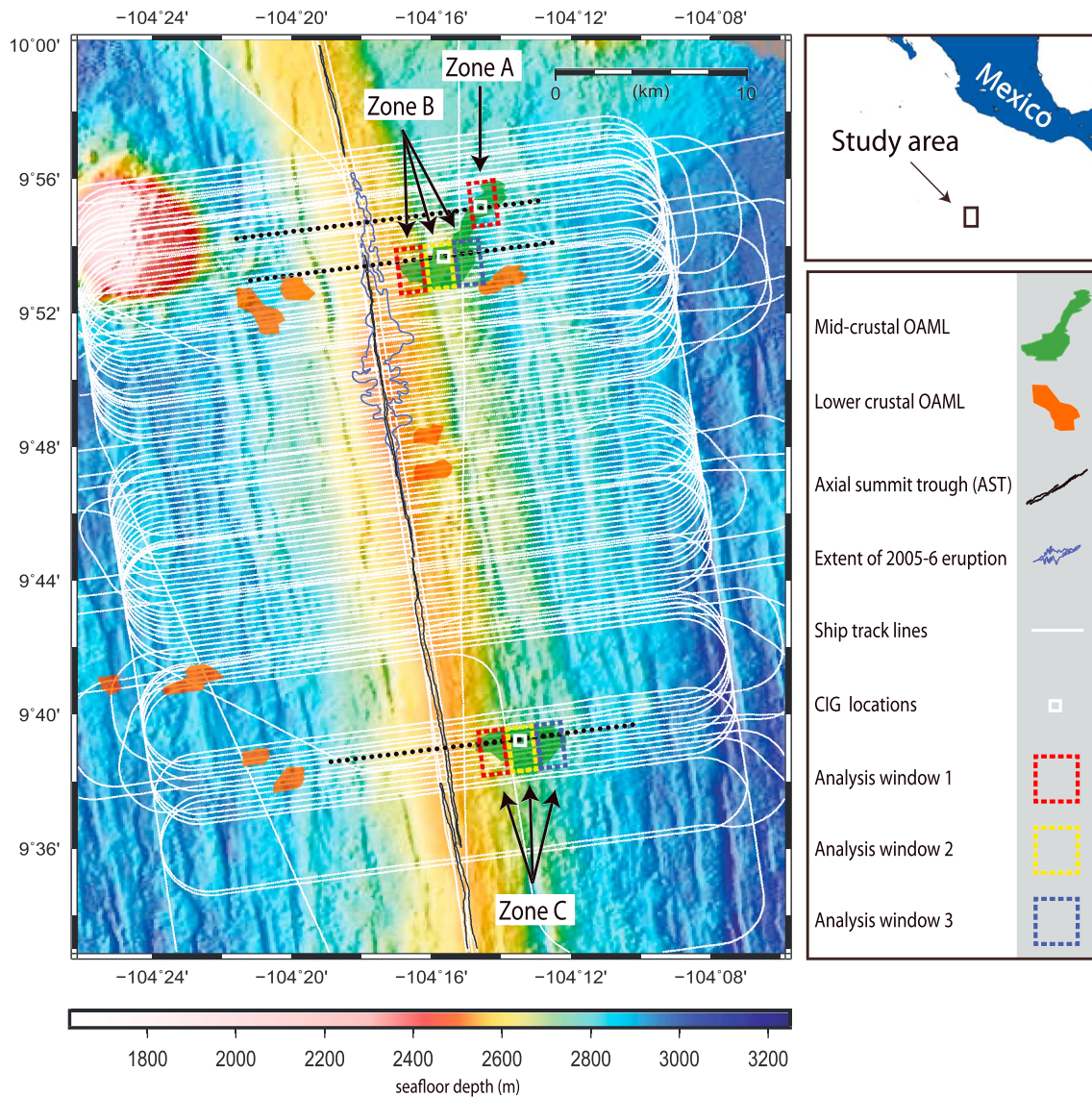


**Figure 1.** Ship track for cruise MGL0812 shown with thin white lines superimposed over the EPR bathymetry (color background) between 9°34.5'N and 10°N latitude. Dotted black lines indicate the surface trace of the three inlines extracted from the 3-D migrated volume and shown in Figures 2 and 3. These inlines cross the two large midcrustal OAMLs. Red, yellow, and blue dashed rectangles outline seismic analysis windows 1, 2, and 3, respectively, within midcrustal OAML Zones A, B, and C investigated in this study. Axial summit trough (AST) is as interpreted by Soule *et al.* [2007]. Extent of 2005–2006 eruption is from Soule *et al.* [2009].

Smith *et al.*, 2001; Goss *et al.*, 2010]. In addition to the axial zone, off-axis lavas have been sampled at several locations [e.g., Perfit *et al.*, 1994; Sims *et al.*, 2003]. From 9°48'N to 9°52'N, the off-axis lavas sampled to ~4 km from the axis on both flanks have U-series model ages that appear to be younger than those predicted by steady state spreading rate models [Sims *et al.*, 2003]. Similarly, anomalously young ages for most samples collected ~4 km away from the axial summit trough (AST) at 9°31'N have been determined by means of <sup>238</sup>U-<sup>230</sup>Th and <sup>235</sup>U-<sup>231</sup>Pa dating techniques [Goldstein *et al.*, 1994]. These results suggest that a portion of the lavas were erupted outside the axial neovolcanic zone generally considered to be ~3 km wide [e.g., Macdonald, 1998; Carbotte *et al.*, 1997].

A bright reflection originating from the midcrustal AML and interpreted to mark the top of the axial low-velocity zone has been identified in the study area by earlier 2-D MCS experiments [e.g., Herron *et al.*, 1980; Detrick *et al.*, 1987; Harding *et al.*, 1993; Kent *et al.*, 1993] and is clearly imaged with the 3-D MCS data [Canales *et al.*, 2012; Aghaei *et al.*, 2014; Han *et al.* 2014] used in this study. This bright reflection is visible beneath most of the axis of the EPR between Siqueiros and Clipperton transform faults and lies at an

average depth of 1.6 km below seafloor (bsf) [Carbotte *et al.*, 2013]. The width of the AML reflector varies from ~0.5 to ~2.0 km [Canales *et al.*, 2012; Aghaei *et al.*, 2014]. Vertically stacked subaxial melt lenses are also imaged in the lower crust using along-axis swath-3-D MCS data also acquired during the 2008 survey [Marjanović *et al.*, 2014].

The thickness and melt content of the AML have been quantitatively constrained at 9°39'N [Hussenoeder *et al.*, 1996] with waveform modeling and at 9°39.3'N, 9°48'N [Collier and Singh, 1997, 1998], 9°42.8'N, and 9°49.1'N [Xu *et al.*, 2014] using 1-D waveform inversion. The results show that the AML is from 30 to 80 m thick with melt content that varies from <40% to >80%. Relative variations in the AML melt content have also been constrained within the investigated section of the EPR by using the along axis swath-3-D MCS data collected from the Siqueiros to the Clipperton transforms. This was done by applying AVA crossplotting analysis technique and *P* wave and *P-S-P* converted wave partial offset stacking [Marjanović, *et al.*, 2015; Xu *et al.*, 2014]. From 2-D partial offset stacking of a subset of the swath 3-D MCS data from 9°30'N to 10°N, Xu *et al.* [2014] interpreted four prominent 2–4 km long melt-rich AML zones spaced 5–10 km from each other. Detailed AVA results from Marjanović *et al.* [2015] show that the three AML segments underlying the 2005–2006 eruption lava flow (~9°45'N to 9°56'N) have variable melt content on an even finer scale with 25% of their total length interpreted as solid to mushy, 37% percent as mostly molten, and 38% as highly molten.

Intracrustal OAMLs of variable shape, surface area, and depth (midcrust and lower crust) have also been identified within the study area (Figure 1) [Canales *et al.*, 2012; Aghaei *et al.*, 2014; Han *et al.*, 2014] using the same 3-D MCS data analyzed in this work. Two prominent midcrustal OAMLs are observed to the east of the ridge axis on the Cocos plate. The first one, centered at ~9°38'N, is imaged at an average two-way traveltime (TWTT) of ~0.75 s bsf and extends from ~1.2 km to ~5.9 km away from the ridge axis. The detailed structure of this OAML is discussed in Han *et al.* [2014]. The second midcrustal OAML is located between ~9°52'N and ~9°56'N and imaged at ~0.75 s TWTT bsf, with its western (closer to the ridge axis) portion found at shorter (0.7 s) and its eastern portion found at longer (0.8 s) TWTTs. This OAML is the focus of the Canales *et al.* [2012] study.

The lower crustal OAMLs are spatially smaller, more abundant, and have a broader range of TWTTs. Four lower crustal OAMLs are found east of the ridge axis. The OAML at ~9°52.5'N is present at ~7.5 km east of the ridge axis at ~1.35 s TWTT bsf. Two deeper OAMLs are found at ~9°48'N and centered ~1.5 km from the ridge axis at 1.8 s TWTT bsf. The shallowest OAML is found at TWTT of ~1.3 s bsf and is located below the large southern midcrustal OAML from ~2.5 km to ~5.0 km away from the ridge axis. Six lower crustal OAMLs are found west of the ridge axis. Two of these OAMLs between ~9°52'N and 9°53'N are centered ~5 km and ~3.5 km from the ridge axis at 1.22 and 1.75 s TWTT bsf, respectively. The OAML centered at ~12 km from the ridge axis at ~9°41'N appears at ~1.64 s TWTT bsf. The spatial extent of the smaller OAML ~4 km farther west is not fully determined due to limited data coverage. Two southernmost OAMLs on the western flank with an average TWTT of ~1.4 s bsf are found ~8 and ~10 km from the ridge axis between ~9°37.5'N and 9°39'N.

### 3. Data Preparation for AVA Analysis

The preprocessing sequence applied for the AVA analysis was focused on preserving the relative amplitudes of the seismic data while retaining the broadest possible signal frequency band. Additionally, because AVA equations are derived for a horizontally stratified Earth, AVA analysis is carried out on common image gathers (CIGs) rather than on common midpoint gathers [Yilmaz, 2001]. The chosen prestack data preprocessing for AVA analysis included 1-D bandpass filtering, 2-D filtering using the LIFT approach [Choo *et al.*, 2004], offset-dependent spherical divergence correction, surface-consistent amplitude balancing, and trace editing. The LIFT method, which is a robust amplitude-preserving approach for noise removal, is recommended when the target of processing is rock property estimation. After prestack data preparation, 3-D Kirchhoff prestack time migration was applied to the data. The migration aperture was 2.5 km in both the inline and the cross-line directions. During the Kirchhoff summation, the amplitudes were multiplied by true amplitude weights using the procedure of Peles *et al.* [2001] to recover the true reflection amplitudes. The computed weight function corrects for the geometrical spreading effects during migration assuming straight ray approximation. To minimize the effect on amplitudes due to limitations of the straight ray approximation, a single weight function was applied to the entire data set and detailed migration velocity analysis was carried out.

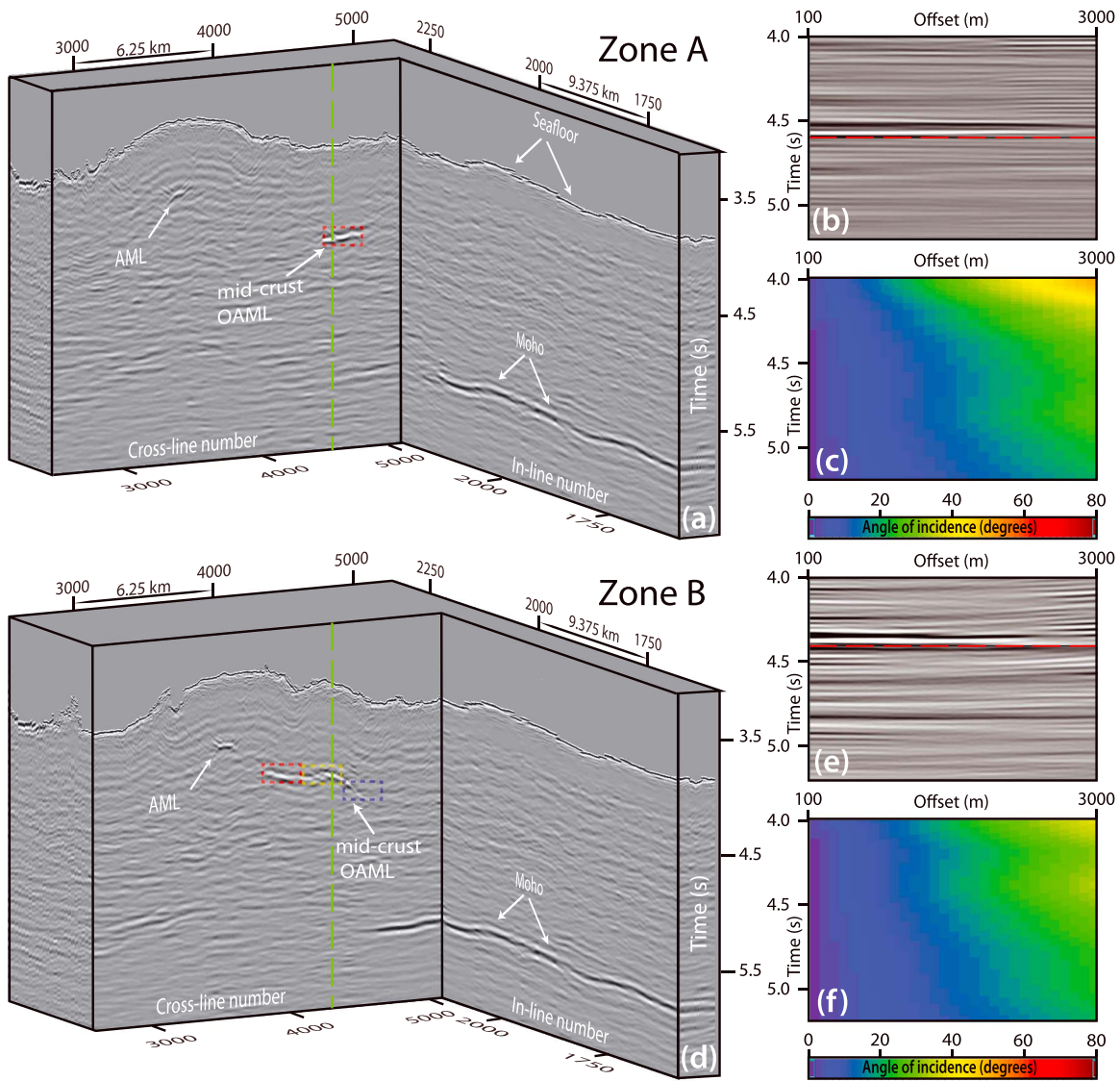


**Figure 2.** Single inlines crossing OAML Zones (a) A and (d) B extracted from the 3-D migrated volume are shown with sample CIGs (b and e) from these inlines and the (c and f) corresponding plots of the angle of incidence. Inlines 2224 and 2128 (Figures 2a and 2d) together with crossline 5120, where the AML, midcrustal OAML, and Moho reflections are shown with white arrows. The green dashed line at crossline 4552 in Figure 2a marks the location of the CIG shown in Figure 2b, while the one at crossline 4288 in Figure 2d marks the location of the CIG shown in Figure 2e. The dashed red, yellow, and blue rectangles in Figure 2d show the individual AVA analysis windows 1, 2, and 3, respectively. A single red rectangle indicates the only analysis window in Figure 2a. (c and f) The maximum offset is limited to 3 km, and the later arriving part of the midcrustal OAML reflection is marked with dashed red lines.

The resultant prestack time migration gathers or CIGs were analyzed after applying LIFT to remove the noise masking OAML and Moho reflection events.

For LIFT, which was simplified so as not to include the signal-add-back step, the CIGs were first divided into low-frequency (0–8–15 Hz) and high-frequency (15–22–200–220 Hz) trapezoidal bands. A residual mid-frequency (8–15–15–22 Hz) range was obtained by subtracting the low- and high-frequency components from the full spectrum. Division into three frequency bands is applied to separate the data into components with different signal-to-noise ratios and different types of noise. This allows for both optimal signal preservation and noise suppression through application of filtering sequences that are tailored for specific frequency bands. An FX filter was applied to the low-frequency band followed by a median filter applied to the data in all frequency bands. All the individual frequency bands were summed at the end to give the processed CIGs that were used for AVA analysis.

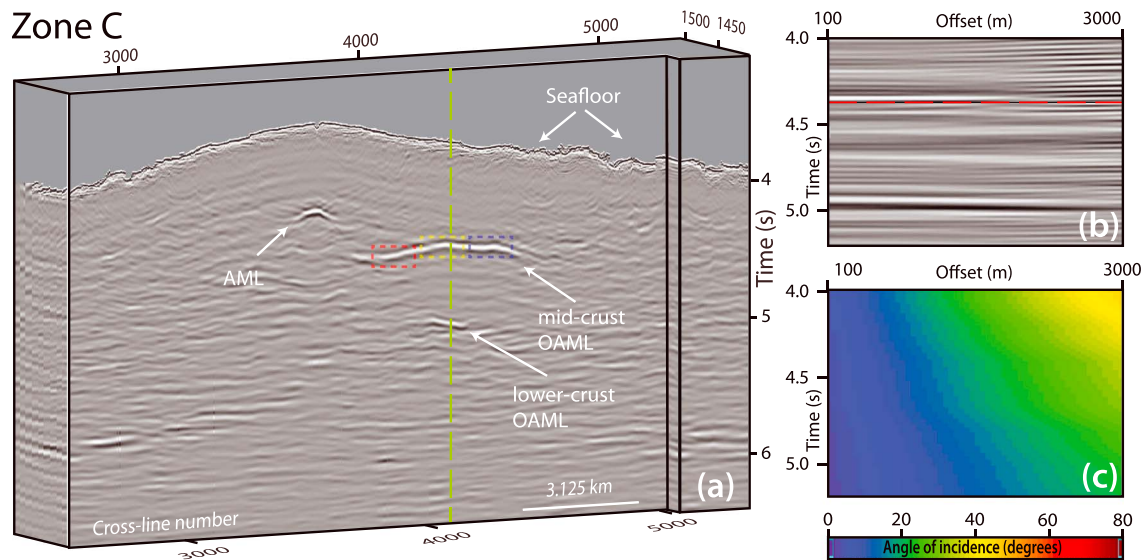


**Figure 3.** (a) Inline 1429 from OAML Zone C is shown with a sample CIG at (b) crossline 4163 and (c) its corresponding plot of the angle of incidence. All other information is the same as in Figure 2.

The targets chosen in this work for the AVA analysis were centered on the midcrustal OAMLs because the  $P$  waves reflecting from them exhibit high signal-to-noise ratio, which is not the case for most of the deeper lower crustal OAMLs. The midcrustal OAML events from the prestack time migrated reflection volume with high signal-to-noise ratio are shown in Figures 2a, 2d, and 3a for each of the investigated Zones A, B and C respectively (see Figure 1 for location). Also shown in Figures 2 and 3 are examples of moveout-corrected CIG gathers from Zones A, B and C (2b, 2e, and 3b, respectively), together with the corresponding reflection angles of incidence (2c, 2f, and 3c, respectively) for the targeted OAML events.

## 4. AVA Analysis

### 4.1. Background

Phase change from solid to fluid has a profound effect on elastic wave velocity, in particular on the velocity of  $S$  waves [Anderson and Spetzler, 1970; Mavko, 1980; Carlson, 2001], therefore strongly affecting the AVA pattern of  $P$  waves reflected from a crustal magma lens. Shown in Figure 4 are the AVA patterns of reflected  $P$  waves from the tops of partially molten ( $V_p = 3.0$  km/s,  $V_s = 2.0$  km/s, and  $\rho = 2700$  kg/m<sup>3</sup>) and fully molten ( $V_p = 2.9$  km/s,  $V_s = 0$ , and  $\rho = 2700$  kg/m<sup>3</sup>) magma lenses [Murase and McBirney, 1973]. Background gabbro velocity ( $V_p = 7.0$  km/s;  $V_s = 3.75$  km/s) and density ( $\rho = 2900$  kg/m<sup>3</sup>) are from Iturrino *et al.* [1991]. These AVA signatures show that the change in amplitude with increasing angle of incidence of the  $P$  wave reflected off a magma lens varies significantly as a function of its melt content, which suggests that the AVA analysis can provide some insight on the melt content of OAMLs [e.g., Singh *et al.*, 1998].

In this work, we take advantage of the strong change in the  $P$  wave AVA signature of a magma lens as a function of melt content (Figure 4) and apply two complementary analysis methods, partial angle stacking and AVA crossplotting, to assess the melt content of the midcrustal OAMLs in Zones A, B, and C shown in Figure 1. In the partial angle  $P$  wave stacking method, limited angle stacks are created, displayed, and analyzed. The information obtained by this method is only qualitative but is insightful [e.g., Carlson, 2001]. Unlike some of the earlier melt content studies targeting the AML [e.g., Singh *et al.*, 1998; Canales *et al.*, 2006], including those across our study area [Xu *et al.*, 2014; Marjanović *et al.*, 2015], we do not make use of the  $P$ - $S$ - $P$  converted waves reflected from OAMLs because they are not present or are too weak to confidently identify in the partial angle stack sections.

Knott-Zoeppritz equations [Zoeppritz, 1919] fully describe the amplitude versus incidence angle behavior of reflected and transmitted elastic waves that arise at a contact between two isotropic homogenous elastic half spaces due to an impinging plane wave and therefore provide a theoretical framework for AVA

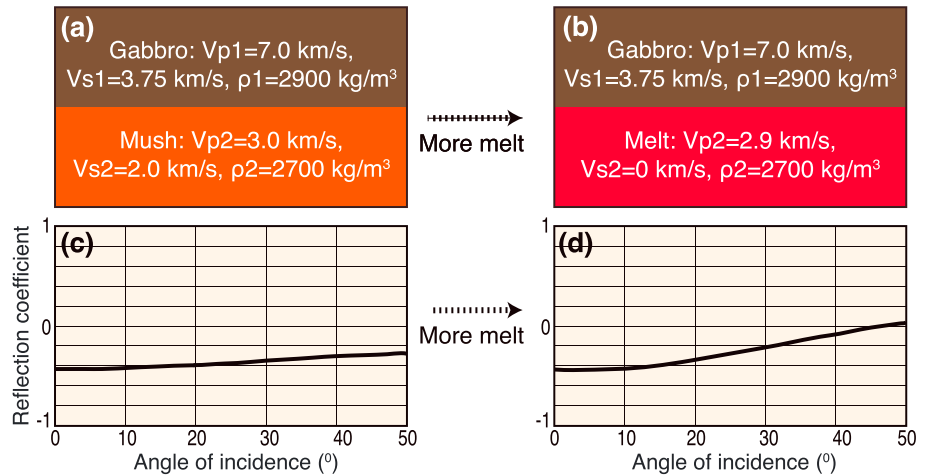


**Figure 4.** Two schematic OAML interface models with crustal gabbro background and associated reflection coefficients plotted as a function of the angle of incidence. (a) In the first model, mush is assumed within the OAML. (b) In the second model, pure melt is assumed to fill the OAML. (c) Reflection coefficient of reflected *P* wave from gabbro/mush interface for angle of incidence from 0° to 50°. (d) Reflection coefficient of reflected *P* wave from gabbro/melt interface for angle of incidence from 0° to 50°.

investigations. These equations are governed by the elastic parameters defining the first (overlying) medium:  $V_{p1}$ ,  $V_{s1}$ , and  $\rho_1$ , and those defining the second (underlying) medium:  $V_{p2}$ ,  $V_{s2}$ , and  $\rho_2$  where  $V_p$ ,  $V_s$ , and  $\rho$  denote compressional wave velocity, shear wave velocity, and density, respectively. However, due to their complexity, Knott-Zoeppritz equations have seen little direct use [e.g., *Yilmaz*, 2001], and linearizing equations [e.g., *Aki and Richards*, 1980] are routinely implemented instead [*Marjanović et al.*, 2015].

For angles of incidence smaller than 30°, *Shuey* [1985] showed that the *P* wave reflection coefficient  $R$  can be approximated by

$$R(\theta) = A + B \sin^2(\theta). \tag{1}$$

In this equation,  $\theta$  is the angle of incidence, and  $A$  and  $B$  are called seismic attributes. The reflection-coefficient or AVA intercept ( $A$ ) is the acoustic term and is a measure of the normal incidence reflection amplitude, while the reflection-coefficient or AVA gradient ( $B$ ) is related to the average Poisson's ratio of the upper layer and lower layer [*Castagna and Swan*, 1997] and is therefore a function of both *P* and *S* wave velocities.

The range of angle of incidence used for AVA analysis in this study was limited to 30° because the *Shuey* [1985] approximation to the Zoeppritz equations is only valid for angles of incidence of less than 30°. The angles of incidence were computed using the 3-D velocity model developed during the migration velocity analysis (Figures 2 and 3).

#### 4.2. *P* Wave Partial Angle Stacking

Partial angle stacks provide a robust and quick way of evaluating AVA responses and identifying anomalous regions along a given horizon [e.g., *Bacon et al.*, 2007]. In this method, partial stack volumes for a chosen range of the angle of incidence, or in the earlier studies partial source-receiver offset range, are produced and inspected visually. Partial angle stack amplitudes are, just like those for full-offset stacks, normalized by the number of contributions to each sample.

Identifying the range of angle of incidence for creating partial stacks that best show the AVA character is important. Analysis of Figure 4, taking into account that *Shuey's* [1985] approximation is valid for angles up to 30°, indicates that the optimal range of angle of incidence for creating near-normal stacks is from 0° to ~20° and for midangle stacks from ~20° to 30°. This is in agreement with incidence angle ranges used for investigations of sedimentary interfaces for petroleum exploration [e.g., *Foster et al.*, 2010] and what was used for the first AVA study of an AML presented in *Marjanović et al.* [2015]. We use these predetermined optimal ranges of angle of incidence (0°–20° and 20°–30°) to produce near-normal and midangle *P* wave partial angle stacks for the targeted Zones A to C of the two investigated midcrustal OAMLs.

### 4.3. AVA Crossplotting

For AVA crossplotting, the seismic attributes  $A$  and  $B$  need to be calculated first. This calculation is done on all CIGs belonging to selected portions of the 3-D seismic volume, with the event of interest (in this case the OAML reflection) flattened. For each CIG,  $A$  and  $B$  are calculated via a least squares inversion of equation (1) (Shuey approximation) for every sample within the chosen analysis time window.

*Castagna et al.* [1998] have shown that crossplotting  $A$  and  $B$  facilitates AVA interpretation. In this interpretation framework, each  $(A, B)$  pair maps into a point in the  $A$ - $B$  plane delineating a pattern dependent on the AVA behavior characterizing the interface under consideration. Depending on the distribution pattern of the  $(A, B)$  pairs in the  $A$ - $B$  plane, four AVA classes (I, II, III, or IV) have been defined. The AVA classes I, II, and III were originally proposed for gas sands by *Rutherford and Williams* [1989] and later extended by *Castagna and Smith* [1994] to include class IV.

For brine-saturated clastic rocks interbedded with shale, there is a well-defined relationship between  $A$  and  $B$  known as the “background” trend in the AVA crossplot plane [*Castagna and Swan*, 1997]. This relationship was developed based on the work by *Gardner et al.* [1974] who showed that there generally is an approximately linear relationship between  $P$  wave velocity and density, and later *Castagna et al.* [1985] who demonstrated that there is a similar (linear) relationship between  $P$  and  $S$  wave velocities in brine-saturated sandstone and shale. In a given time window, deviations from this background trend are indicative of hydrocarbons or unusual lithologies. Developing background trends in the  $A$ - $B$  plane for other interface lithologies is critically important because it provides an extended framework for interpretation of the computed AVA attributes.

The relationship between  $A$  and  $B$ , assuming arbitrarily large velocity contrasts and negligible density changes along a reflecting interface, can be expressed as follows [*Foster et al.*, 2010]:

$$B = (1 - 8\gamma^2)A - 4\gamma\Delta\gamma(1 - \Delta\gamma) + (1 - 2\gamma)O(A^2) \quad (2)$$

where  $\gamma = \frac{\langle V_s \rangle}{\langle V_p \rangle} = \frac{V_{s1} + V_{s2}}{V_{p1} + V_{p2}}$  and  $\Delta\gamma = \frac{\Delta V_s}{\langle V_s \rangle} - \frac{\Delta V_p}{\langle V_p \rangle}$  (neglecting second-order terms).

For small perturbations in elastic properties at a reflecting interface, *Foster et al.* [2010] showed that the above relation can further be simplified to

$$B = \left(1 - 8\left(\frac{V_s}{V_p}\right)^2\right)A \quad (3)$$

In this equation,  $V_p$  and  $V_s$  are the average  $P$  wave and  $S$  wave velocities of the two media  $\left(\frac{V_{p1} + V_{p2}}{2}$  and  $\frac{V_{s1} + V_{s2}}{2}\right)$ .

This equation implies that lines of constant  $\frac{V_p}{V_s}$  pass through the origin. Furthermore, the slope of the predicted background trend depends only on the background  $\frac{V_p}{V_s}$  ratio. As  $\frac{V_p}{V_s}$  increases, the slope of the background trend becomes more positive, or the trend rotates counterclockwise for the AVA intercepts ( $A$ ) plotted along the  $x$  axis [*Castagna et al.*, 1998]. In their AVA investigation of the AML in the same area of the EPR, *Marjanović et al.* [2015] observed that the data point clouds for this geologically similar target are centered on the origin. This validates the assumption given in equation (3) and allows for interpretation of  $A$ - $B$  crossplots in the framework of a simple linear relationship.

Various constant ratios of  $V_p$  over  $V_s$  can be used to define the background trends. However, the relation between elastic parameters as a function of melt percentage in gabbroic rocks is complex [*Caricchi et al.*, 2009], and extracting background trends in the intercept-gradient plane is not straightforward. We use the *Hashin and Shtrikman* [1963] bounds to calculate the  $\frac{V_p}{V_s}$  background trends needed to provide an interpretational framework for the AVA crossplots. These background trends allow us to interpret the results from the AVA crossplotting technique in terms of the OAML melt content, which is a step forward in quantifying magma melt content from the work carried out by *Marjanović et al.* [2015]. The *Hashin and Shtrikman* [1963] bounds provide constraints on the upper and lower velocity limits for varying fractions of melt. However, it is important to note that the *Hashin and Shtrikman* [1963] is a theoretically derived relationship and, as such, has limitations. This relationship assumes isotropic media, was tested experimentally only on a single two-phase alloy (tungsten carbide-cobalt), and requires in situ knowledge of material velocities when completely solidified and molten.

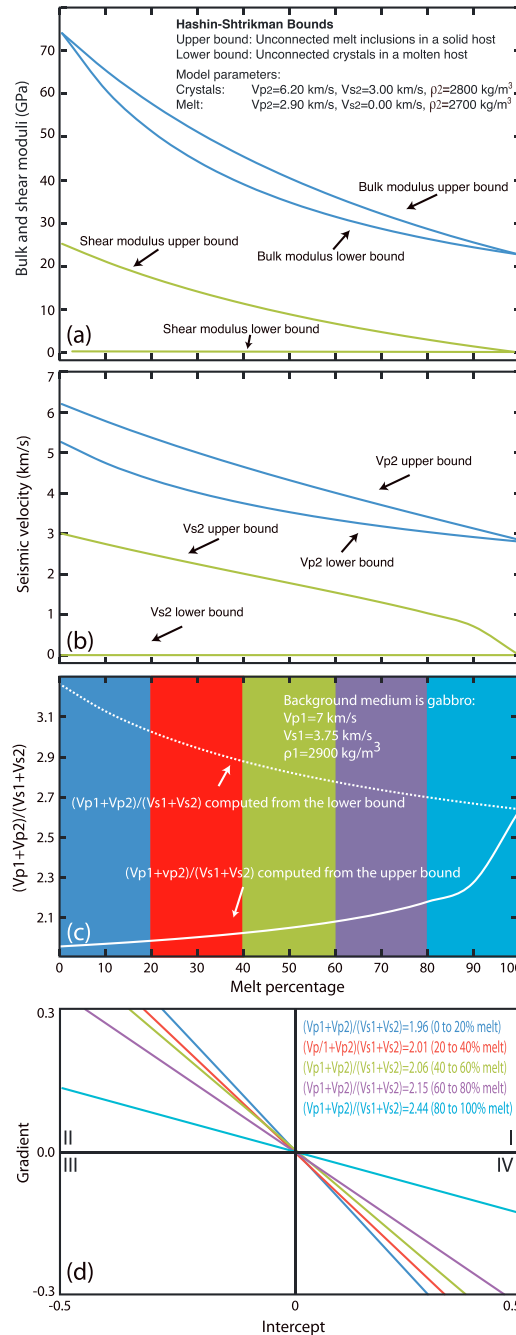


**Figure 5.** A framework for interpreting AVA crossplot results and estimating melt percentage using the Hashin-Shtrikman bounds. (a) Bulk and shear moduli upper and lower bounds as a function of melt fraction computed for a two-phase material for unconnected melt inclusions in a solid host (upper bounds) and unconnected crystals in a molten host (lower bounds). (b)  $P$  and  $S$  wave velocities calculated using the lower and upper bounds of elastic properties for melt and crystals given in Figure 5a. (c) Assuming that the background medium is gabbro, the mean  $V_p/V_s$  ratio is computed from the lower velocity bounds (dashed white line) and the upper velocity bounds (solid white line). Color background in Figure 5c shows melt-percentage ranges used for computation of background trends presented in Figure 5d using corresponding colors. (d) The background trends were computed from the mean  $V_p/V_s$  for the upper bound curve for each 20% melt-percentage range. The AVA quadrants are also annotated in Figure 5d.

Following Xu *et al.* [2014], we consider the maximum bound to correspond to an end-member model of unconnected melt inclusions in a solid host, where  $V_p = 6.2$  km/s,  $V_s = 3.0$  km/s, and  $\rho = 2800$  kg/m<sup>3</sup>, and the minimum bound to represent the opposite end-member model of unconnected crystals in a molten host, where  $V_p = 2.9$  km/s,  $V_s = 0$  km/s, and  $\rho = 2700$  kg/m<sup>3</sup>. Figure 5b shows the  $P$  and  $S$  wave velocities computed for different melt percentages following the Hashin and Shtrikman [1963] relation for the physical properties (bulk and shear moduli, Figure 5a) of a two-phase material. We assume gabbro with elastic parameters of  $V_p = 7.0$  km/s,  $V_s = 3.75$  km/s, and  $\rho = 2900$  kg/m<sup>3</sup> [Irrino *et al.*, 1991] for the background medium.

Figure 5c shows the ratio of the average  $P$  wave velocities ( $V_p$ ) to the average of  $S$  wave velocities ( $V_s$ ) of the upper and lower layer computed from the Hashin-Shtrikman bounds. The average ratio is significantly affected by melt percentage. To define the background trends for a range of melt percentages, we use the average  $V_p/V_s$  ratio for the upper Hashin-Shtrikman bound in Figure 5c and compute the mean of this ratio for melt-percentage intervals of 20% across the full melt range of 0 to 100%. This results in the five background trends shown in Figure 5d. We use the upper Hashin-Shtrikman bounds because they are in better agreement with the existing estimates for  $V_p$  and  $V_s$  [Vera *et al.*, 1990; Kent *et al.*, 1993; Singh *et al.*, 1998; Xu *et al.*, 2014]. This is particularly true for low to moderate melt content, for which the  $V_s = 0$  km/s predicted by the lower Hashin-Shtrikman bounds is highly unlikely. Moreover, the background trends computed using the lower Hashin-Shtrikman bounds would fall in quadrants I and III [Rutherford and Williams, 1989], which is at odds

with the amplitude decrease with increasing angle of incidence predicted in Figure 4 and AVA pattern IV [Castagna and Smith, 1994].

Presence of a thin bed, as is the case with most AMLs and is likely the case with OAMLs, complicates the interpretation of the crossplots [Ross, 2000]. Marjanović *et al.* [2015] examine magma lens thin bed tuning effects on the AVA analysis and conclude that in the absence of needed magma lens thickness constraints, the interpretation of the AVA behavior between different magma lenses or their parts has to be carried out in the framework of constant thickness, which means that any AVA signature differences are attributed to variations in the melt fraction only.

The assumption of a single mirror-like interface giving rise to the reflection response of magma reservoirs, the assumptions taken to derive the Hashin and Shtrikman [1963] theoretical relationship, and the use of only the upper Hashin and Shtrikman bound represent the limitations of our approach. These limitations preclude accurate estimation of uncertainties for the computed  $\frac{V_p}{V_s}$  background trends and indicate that best linear fits on *A* and *B* crossplots are, in terms of magma lens melt content, best interpreted in qualitative terms. Nevertheless, the results obtained with the presented approach provide first-order constraints on relative variations in melt content.

## 5. Results

### 5.1. P Wave Partial Angle Stacking Results

Signal envelope calculated from stack data is commonly used as a seismic attribute indicative of the seismic data energy [Taner *et al.*, 1979]. Here we compute signal envelopes of the near-normal stack and midangle stack volumes corresponding to the midcrustal OAMLs of Zones A, B, and C (Figure 1). The computed signal envelopes, created using data with angle of incidence ranges from 0° to 20° and from 20° to 30°, respectively, are shown on sample intersecting inline and crossline pairs for each zone (Figure 6).

Among the three zones, the largest difference between the signal envelope of near-normal stack and midangle stack volumes is found in Zone C (Figures 6e and 6f). The signal envelope on the near-normal stack of Zone C shows strong amplitude that is focused over a short (~50 ms) two-way traveltime window and quickly fades away into the background outside this thin zone. For the same range of inlines and crosslines and the same time window, the signal envelope amplitude is significantly reduced on the midangle stack volume.

The signal envelope of the near-normal stack volume of Zone B (Figure 6c) is significantly larger than the signal envelope of the midangle stack volume for the same range of inlines and crosslines (Figure 6d). Similar to Zone C, the strong envelope amplitudes are found in a short (~50 ms) two-way traveltime window, but for Zone B they appear to weaken more gradually into the background envelope amplitudes.

The signal envelope values of the midangle stack volume of Zone A are smaller than the values for the near-normal stack in this zone (Figures 6a and 6b) but much less so than even for Zone B. Moreover, the strong envelope amplitudes are not as sharply focused but are rather found in a longer (~100 ms) two-way traveltime window and weaken gradually into the background envelope amplitudes.

### 5.2. AVA Crossplotting Results

The selected CIG areas for AVA crossplotting show high signal-to-noise ratio of the OAML reflections (Figures 2 and 3). For Zones B and C, the AVA crossplotting was done for three separate space-time analysis windows to examine melt content variation of the OAMLs as a function of distance away from the ridge axis. The OAML in Zone A is narrower than the OAMLs in Zones B and C, and the crossplotting was performed only in one window where the signal-to-noise ratio is comparable to the signal-to-noise ratio of Zones B and C. The analysis windows in Zones B and C extend for 1250 m in the crossline direction, 900 m in the inline direction, and 100 ms in the vertical direction. The analysis window of Zone A is the same as Zones B and C except that it is 600 m wide in the inline direction. The areal size of the analysis windows was chosen to include as much as possible of the high signal-to-noise ratio OAML reflection response from flatter sections of the OAML where the signal arrives within the 100 ms time window, which was chosen to encompass all of the OAML reflection response and minimize noise inclusion. These analysis windows are shown in Figures 1, 2a, 2d, and 3a.

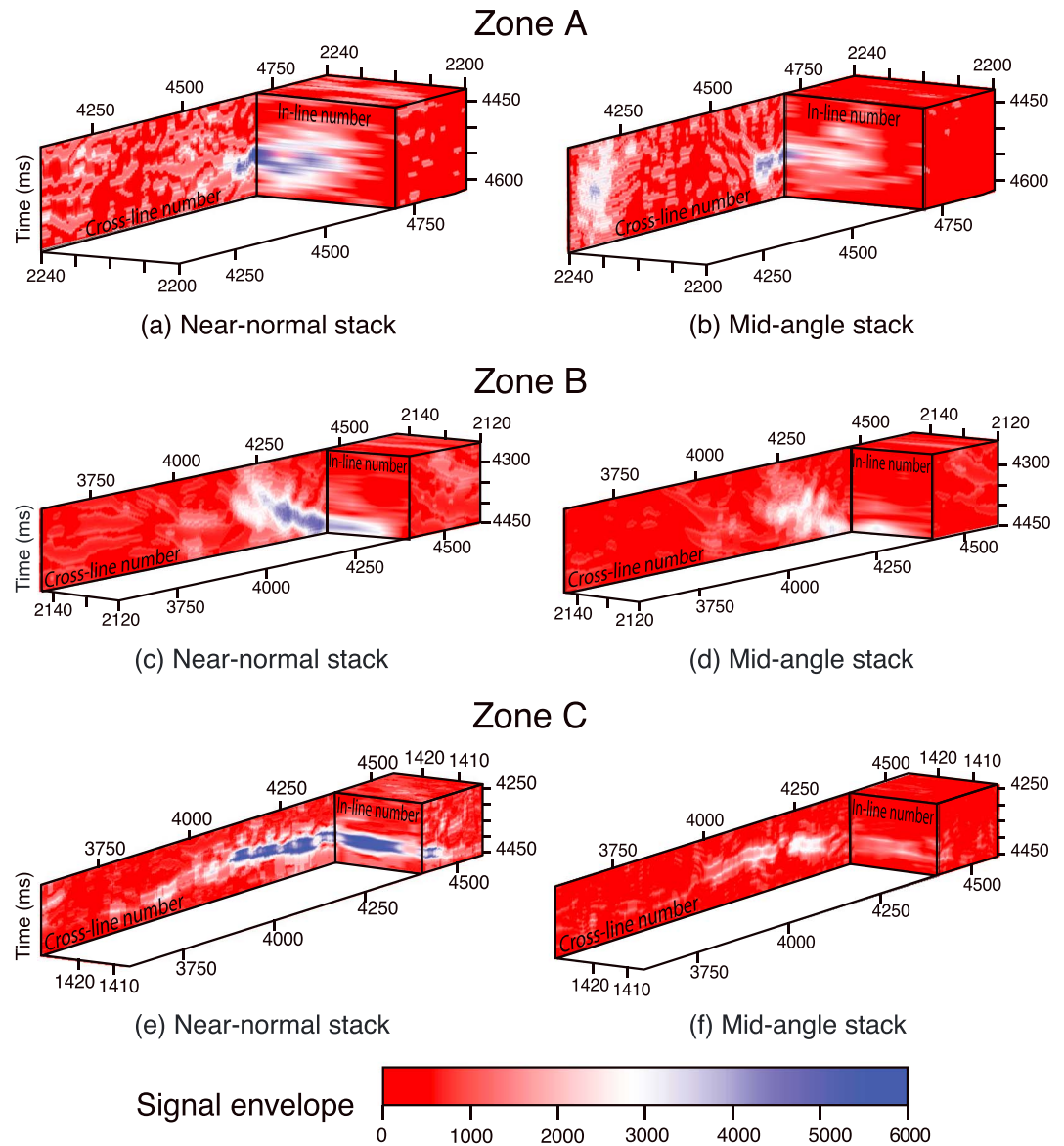


**Figure 6.** Signal envelopes computed from the near-normal stacks (angle of incidence  $0^\circ$  to  $20^\circ$ ) and midangle stacks ( $20^\circ$  to  $30^\circ$ ) for the three zones shown in Figure 1. (a, c, e) Signal envelope for the near-normal stack of Zones A, B, and C, respectively. (b, d, f) Signal envelope for the midangle stack of Zones A, B, and C, respectively. These figures show that the seismic energy of the OAML reflection in the midangle stacks section is significantly less than that for the corresponding near-normal stacks. This pattern of the amplitude decrease with increasing angle of incidence was predicted for the reflected  $P$  wave from the top of a gabbro/mush or gabbro/melt lens in Figure 4.

An example of AVA crossplotting for one of the analysis windows is presented in Figure 7. The crossplotted  $A$  and  $B$  values for this and all the other six analyses windows occur dominantly in quadrants II and IV. This result corresponds to AVA class IV that is characterized by amplitude decrease with increasing angle of incidence. AVA crossplot values occur in quadrants II and IV because for each positive and negative reflection-amplitude pair, two  $A$ - $B$  pairs are computed: one  $A$ - $B$  pair from the positive amplitudes and plotting in quadrant IV, and the second  $A$ - $B$  pair from the negative amplitudes and plotting in quadrant II.

The best fitting  $A$  versus  $B$  linear trends calculated for the crossplotted data for all analyses windows of Zones A, B, and C (see Figure 1 for locations) are shown with solid black lines in Figure 8. To facilitate melt content estimation in each analysis window and interpret the results, the calculated background trends presented in Figure 5d are projected to the  $A$  versus  $B$  crossplot plane. The background trends show a counterclockwise

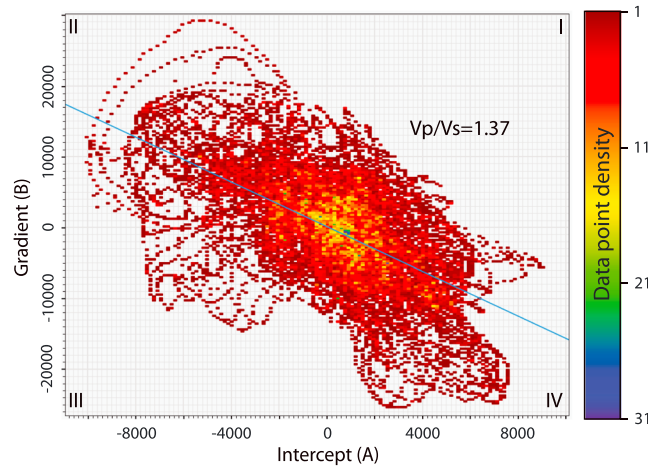


**Figure 7.** Detailed results of AVA crossplotting of intercept (A) and gradient (B) for window 1 of Zone A. Intercept is calculated from the reflection signal with the angle of incidence range from 0° to 20°, and gradient is calculated from the reflection signal with the angle of incidence range from 20° to 30°. Color indicates the density of data points per designated unit area represented by the background rectangles. Blue line is the best linear fit that defines the  $V_p/V_s$  ratio for the window 1 of Zone A.

rotation from melt-poor magma lenses toward melt-rich magma lenses. The  $V_p/V_s$  ratios were calculated from the slope of the best fit trend lines using equation (3) and are listed for all study zones and analysis windows in Table 1. The  $V_p/V_s$  values range from the minimum value of 1.37 for the single analysis window of Zone A to the maximum value of 1.94 in analysis window 1 of Zone C.

## 6. Discussion

The results from AVA crossplotting indicate that the OAMLs on average contain a small amount (<20%) of melt. Geologic possibilities for the low OAML melt content, comparison between the OAML and AML melt content, and the source of melt for the OAMLs are discussed in the following sections and are schematically shown in Figure 9.

### 6.1. Melt Content of Midcrustal OAMLs

The best fitting  $A$  versus  $B$  linear trends plot between the vertical axis ( $A = 0$ ) and the 0–20% background trend (Figure 8) indicating a high crystalline component for the OAMLs. Though  $P$  wave partial angle stacks provide no direct characterization of the investigated OAMLs melt volume, the vertical and lateral transitions in the amplitude of the signal envelope for the near-angle and midangle stacks (Figure 6), and the difference

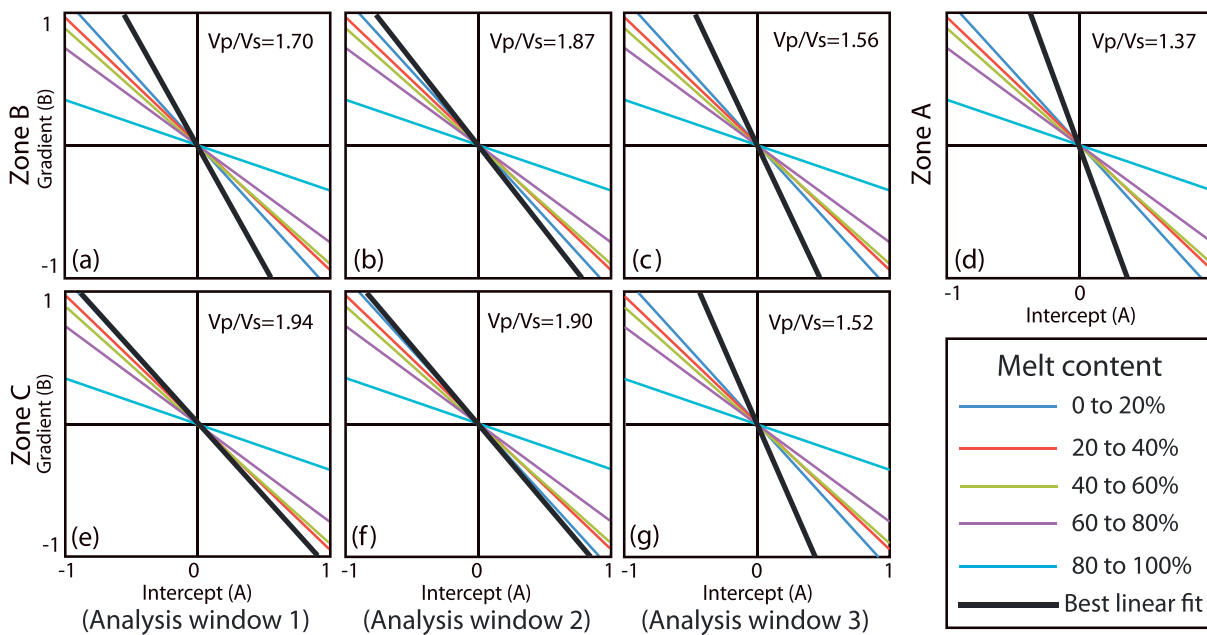


**Figure 8.**  $V_p/V_s$  ratios for all seven analyses windows of Zones A, B, and C computed from the results of crossplotting intercept (A) and gradient (B) are shown with solid black lines representing the best linear fits. (a–c) The  $V_p/V_s$  ratios for the Zone B analysis windows 1, 2, and 3 which are shown with dashed red, yellow, and blue rectangles, respectively, in Figures 1 and 2d. (d) The  $V_p/V_s$  ratio for the single analysis window in Zone A shown in Figures 1 and 2a with a dashed red rectangle. (e–g) The  $V_p/V_s$  ratios for the Zone C analysis windows 1, 2, and 3 which are shown with dashed red, yellow, and blue rectangles, respectively, in Figures 1 and 3a.

**Table 1.** Computed  $V_p/V_s$  Ratios, Background Trends, and Melt Content Interpretation<sup>a</sup>

Analysis Window ↓	$V_p/V_s$ ratio	Background Trends	Melt content	
Zone A	1	1.37	$V_p/V_s=1.55$	Partially molten/solid to mushy $V_p/V_s \leq 2.06$
Zone B	1	1.70	$V_p/V_s=1.70$	
	2	1.87	$V_p/V_s=1.85$	
	3	1.56	$V_p/V_s=2.00$	Mostly molten $2.06 < V_p/V_s \leq 2.15$
Zone C	1	1.94	$V_p/V_s=2.15$	Highly molten $V_p/V_s > 2.15$
	2	1.90	$V_p/V_s=2.30$	
	3	1.52	$V_p/V_s=2.50$	
Average for all windows/zones	1.72			

<sup>a</sup>(left)  $V_p/V_s$  ratios for all seven analyses windows of Zones A, B, and C (see Figure 1 for location) and their averages are shown together with (right) the background trends and the corresponding interpretation for the amount of melt put forward by Marjanović et al. [2015], which is shown as color background. The relationships between the background trends and melt content developed in Marjanović et al. [2015] is empirical in nature (based on available measurements of  $V_p$ ,  $V_s$  and  $\rho$ ), as opposed to the one presented in Figure 5 of this work and based on the Hashin and Shtrikman [1963] theoretically derived relationship.

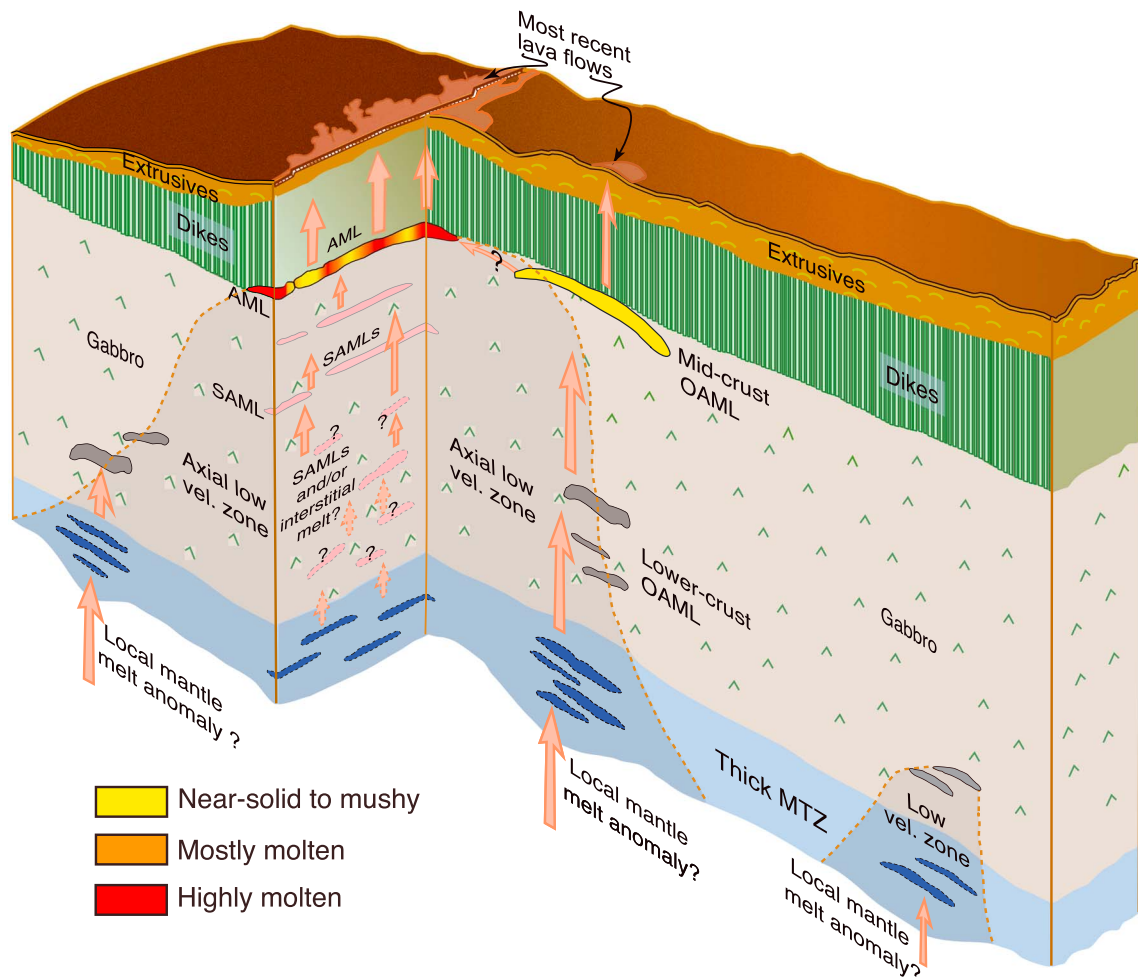


**Figure 9.** Schematic fence diagram showing the AML and OAMLs in crustal sections across and along the ridge axis. Color depicts AML and midcrustal OAML melt content as described in the legend, following the classification of Marjanović et al. [2015]. Subaxial melt lenses (SAMLs), lower crustal OAMLs, and MTZ magma lenses are shown in light purple, gray, and dark blue, respectively, as their melt content is not known. Possible directions of melt migration are shown with pink arrows. A thick MTZ is observed in the axial and near axial region in the area where OAMLs are imaged [Aghaei et al., 2014]. This area may also be characterized by a somewhat wider axial low-velocity zone than observed elsewhere, as shown using shading and dashed brown lines.

between them, provide insight on the relative melt content and distribution and support the AVA crossplotting results. For example, changes in the envelope amplitude are largest and sharpest for Zone C and weakest and most gradual for Zone A, both vertically and laterally (Figure 6). This implies that the melt content is on average most likely largest in Zone C and smallest in Zone A, and that its distribution is most uniform in Zone C and least uniform in Zone A.

The low melt content of the midcrustal OAMLs as determined by the AVA crossplotting may not be surprising given that the 60 km long section of the AML from 9°30'N to 10°N at the EPR is also found to be predominantly melt poor [Xu *et al.*, 2014]. Marjanović *et al.* [2015], using a similar AVA crossplotting approach as the one applied in this work but focused on the central and presumably most melt rich section of the AML, conclude that only 5–10% of the AML from 9°30'N to 10°N is highly molten. In addition, based on the study by Marjanović *et al.* [2015], the AML segments at latitudes of the two midcrustal OAMLs evaluated in this work are estimated to be in a state of crystalline mush.

The most likely possibilities for low melt content of the midcrustal OAMLs include the following: (a) the OAMLs are drained because of off-axis eruptions that preceded our 2008 survey; (b) the OAMLs are feeding the on-axis magmatic systems; and (c) the OAMLs have limited mantle melt supply in comparison to the AML.

#### 6.1.1. Low OAML Melt Content Due To Off-Axis Eruptions

Volcanic edifices oriented parallel to the spreading direction, hundreds of meters in diameter, 30–60 m tall, and extending for 2.4 km from the ridge axis have been observed above the OAMLs in Zone C [Han *et al.*, 2014]. The total volume of these volcanic edifices is ~5.3% of the total extrusive volume amounting to ~0.3% of the total crustal volume in this area. Based on these volume estimates, Han *et al.* [2014] conclude that off-axis eruptions above the OAMLs do not contribute significantly to overall crustal accumulation. Moreover, the limited diameter of these volcanic edifices indicates that the periodic eruptions from this midcrustal OAML may be characterized by small lava volume, but in situ seafloor observation is required to confirm this possibility.

Although there currently is no published bathymetric or morphologic evidence for off-axis eruptions from the OAMLs in Zones A and B (between 9°52'N and 9°57'N), anomalously young ages have been found from studies of basalt samples collected across the EPR to the south from 9°48' to 9°52'N consistent with off-axis eruptions in the past within ~4 km of the spreading center [Sims *et al.*, 2003]. Some investigators suggest that these young lavas sampled off-axis originate within the AST and have been transported several kilometers off-axis via surficial and/or subsurface channels [e.g., Haymon *et al.*, 1993; Waters *et al.*, 2011]. However, this possibility is unlikely for the OAML region because recent submersible dives directly above our Zones A, B, and C (S. M. White, personal communication, 2016) indicate younger lava than for the surrounding crust consistent with seafloor eruptions fed locally by the underlying OAMLs. No evidence for fresh lavas (<1–2 year old based on visual observations of lavas erupted on-axis in 2005–06) were found during these dives however, and the possibility that the low melt content of two OAMLs investigated in this study reflects lens depletion due to recent eruptions is unlikely.

#### 6.1.2. Low OAML Melt Content Due To Feeding of On-Axis Magmatic System

Another possible explanation to account for the melt-poor midcrustal OAMLs is that some of the melt in these magma bodies migrates toward the on-axis magmatic system (Figure 9) [Canales *et al.*, 2012]. Although there is no imaged continuity between the AML and OAML, there are indications of connectivity between these magma bodies (Figure 3a). The eastern end of the AML is located near the western edge of the southern midcrustal OAML (Figure 3a) [Han *et al.*, 2014]. Near vertical or steep-angle magma ascent is expected and may be taking place via highly inclined magma conduits from the western edge of the OAML toward the eastern end of the AML, but we cannot image such steep conduits due to limitations of our data and/or imaging methods applied. In Zone B, melt pockets extending from the northern OAML to the axial low-velocity zone also support some level of connectivity between the axial and off-axis magmatic systems [Canales *et al.*, 2012].

AVA crossplot results in Figure 8 and Table 1 show that the highest average melt concentration, as estimated from  $\frac{V_p}{V_s}$  ratios of windows 2 for Zones B and C, are within the central sections of the OAMLs. Beyond the apex region, analysis windows 1, found closer to the ridge axis for both Zones B and C, have greater ratios than windows 3 that are found farther away from the ridge axis and have the smallest average ratio. This suggests that for the two investigated midcrustal OAMLs, peripheral melt may be preferentially accumulating at

the edges nearest the ridge axis. Upward migration of the melt from this area toward the shallow central regions of the concave shaped OAML and potentially the AML is likely considering the buoyancy of melt in the crust [Canales *et al.*, 2012; Han *et al.*, 2014]. For a quasi-stationary mantle source, we expect the melt to be intruded from below the western OAML edge as the crust is transported away from the axis resulting in preferential accumulation of peripheral melt at the edge nearest the ridge axis. Intriguingly, while the estimated melt contents are about the same for analysis windows 2 covering the central portions of Zone B and Zone C, analysis window 1 of Zone B has less melt than the same analysis window of Zone C. Perhaps, melts were tapped from this region during the 2005–2006 AML eruption at the EPR (9°46′–9°56′N) accounting for lower melt content in this nearest ridge section of the northern OAML recorded in 2008 by our MCS survey. However, the volume of the melt that the OAMLs contribute to the AML eruptions is probably not a significant fraction of the overall melt that erupts at the ridge axis because otherwise lavas formed by AML and OAML eruptions would not have distinct geochemical signatures.

### 6.1.3. Low OAML Melt Content Due To Limited Mantle Melt Supply

The most likely primary cause for low melt content of the OAMLs, relative to the AML, is more limited melt supply from the underlying mantle source reservoir. Based on inferred crustal thickness anomalies associated with the southern OAML and volume estimates of the volcanic constructs located above this feature, Han *et al.* [2014] conclude that the OAML contribution to total crustal thickness is small (~3%). Unlike the AML, which is believed to be a quasi steady state body, the OAMLs are likely to be ephemeral melt-poor bodies due to this implied limited melt supply from the underlying mantle source reservoirs. The limited melt supply, combined with potential loss of some melt due to migration toward the AML, may also result in a significantly longer period of melt replenishment for OAMLs throughout their life span in comparison to the AML. This would lead to partial crystallization at peripheral sections of these lenses due to the long cooling interval and OAML eruption recurrence rates that are lower than for the AML. However, Canales *et al.* [2012] estimate that it would take only 8 to 12 years for an OAML to solidify if intruded into cold and fully solidified crust, taking into account hydrothermal heat removal, which suggests that some fraction of OAMLs are single melt intrusion events.

## 6.2. OAML Versus AML Melt Content Estimates

An additional source contributing to the difference in the estimated OAML melt content from this work and the AML melt content from Marjanović *et al.* [2015] is related to the methodology rather than geology. The work presented here is the first 3-D AVA study of the melt content of a magma lens. Because of the irregular shape of the investigated OAMLs and the rectangular shape of the chosen AVA analysis window, all windows cover both central (inner) and peripheral (outer) sections of the investigated OAMLs. The ratio between central and peripheral OAML sections is highest for windows 2 of Zones B and C and smallest for window 1 of Zone A. The computed melt estimate for each analysis window, therefore, represents the average melt content across an area that includes both central, relatively melt rich, and peripheral sections of an OAML, where melt content diminishes to 0% at the edges. This is in contrast to the quantitative MCS studies of AML melt content carried out so far in 1-D [Hussenoeder *et al.*, 1996; Collier and Singh, 1997, 1998; Canales *et al.*, 2006; Xu *et al.*, 2014] and 2-D [Marjanović *et al.*, 2015], in which melt content estimates were limited only to the central part of the targeted magma lenses. These central parts of the targeted AMLs were defined by the strongest reflection response observed, generally arising from the topographic highs of magma lenses that are presumed to contain the highest fraction of melt. For example, adjacent to our study area, the 2-D analysis of Marjanović *et al.* [2015] is centered on the axis parallel common midpoint line following the middle of the AML that is presumed to straddle the line of maximum AML melt content. Additionally, the data used for AVA analysis of the AML and the OAML, carried out by Marjanović *et al.* [2015] and in this work, were collected along and across the ridge axis, respectively, but possible effects of anisotropy on the results were not taken into account. As a result, it is not possible to carry out a direct comparison of the estimates of OAML melt content presented here and the results from the earlier 1-D and 2-D studies of the AML. However, a relative comparison of the AML and OAML melt content, as determined by the AVA crossplotting study of the AML [Marjanović *et al.*, 2015] and of the two large midcrustal OAMLs carried out in this work, is possible.

Table 1 lists  $V_p/V_s$  ratios for all seven analyses windows of Zones A, B, and C computed from the results of AVA crossplotting and compares them with the background trends from Marjanović *et al.* [2015], which are based on available measurements of  $V_p$ ,  $V_s$ , and  $\rho$ . These authors divide the background trend range in three areas and interpret them to be indicative of magma lenses that are partially molten, mostly molten, and highly

molten. Following the interpretation of the background trends put forward by *Marjanović et al.* [2015], the OAMLs covered by the analysis windows fall within the family of trends that represents partially molten (solid to mushy) material. Table 1 also shows the average  $V_p/V_s$  ratio for all seven OAML analysis windows that, as would be expected, also falls within the trend range area thought to be representative of partially molten magma. The average  $V_p/V_s$  ratio for the AML in the study area computed from the results presented in *Marjanović et al.* [2015] is 2.07 and falls right at the boundary between trend areas interpreted as being indicative of partially molten and mostly molten magma. These average  $V_p/V_s$  ratios for the AML and OAMLs, when interpreted using the background trends computed from upper Hashin-Shtrikman bounds (Figure 5), suggest that on average the investigated OAMLs contain <20% melt and that the AML contains about 50% melt.

The computed  $V_p/V_s$  averages point to the larger average melt content of the AML in the study area than the average melt content of the two large midcrustal OAMLs at the time (2008) the data were collected. In support of this result, strong *P-S-P* converted wave phases have been observed at regions along the axis of the EPR where the AML contains highest percentage of melt. The converted phases are strongest on the mid-angle range and are hardly seen on near-angle range. In addition, the stacking velocity of these events is lower than the stacking velocity for the AML [e.g., *Xu et al.*, 2014]. No such converted phases have been observed in Zones A, B, and C, further indicating that the midcrustal OAMLs contain less melt than the AML and backing the results of the AVA crossplotting analysis. However, because the exact melt percentage of the investigated magma bodies cannot be confidently determined due to the limitations of the developed background trends, neither can the difference in their melt content be accurately quantified. Moreover, the difference in the average melt content between the AML and the OAMLs is likely smaller than the results suggest because the average  $V_p/V_s$  ratio, and therefore the interpreted melt content of the AML, may be overestimated by the *Marjanović et al.* study because this study is 2-D and focused only on the AML apex, as elaborated earlier.

### 6.3. Melt Source of the Midcrustal OAMLs

The two most plausible melt-source reservoirs for the investigated OAMLs [*Han et al.*, 2014] are (1) the broad zone of melt accumulation within and beneath the Moho transition zone (MTZ) that feeds the ridge-axis magmatic system, and (2) local melt anomalies in the underlying shallow mantle.

Seismic and compliance studies at the EPR indicate the presence of a broad subcrustal melt reservoir 10–20 km wide and centered about the ridge axis with 3–11% melt fraction within and beneath the MTZ, possibly distributed in sills (Figure 9) [*Garmany*, 1989; *Dunn et al.*, 2000; *Crawford and Webb*, 2002; *Toomey et al.*, 2007]. This subcrustal melt reservoir is likely a general feature of intermediate-to-fast spreading centers, with its melt content being a function of magma supply to the ridge [*Canales et al.*, 2014]. The width of this region is consistent with the distance over which OAMLs are observed [*Canales et al.*, 2012; *Aghaei*, 2013; *Han et al.*, 2014]. Analysis of the 3-D MCS data set used in this work shows that the MTZ reflection character in the area varies among impulsive, shingled, and diffusive [*Aghaei et al.*, 2014]. Both the impulsive and shingled Moho types are single-phase reflection responses that are thought to arise from thin MTZs, while thick MTZs (Figure 9) are believed to generate the diffusive Moho type that is characterized by a multiphase reflection response [*Brocher et al.*, 1985; *Collins et al.*, 1986; *Nedimović et al.*, 2005]. The cause for the thick MTZ is thought to be less efficient mantle melt delivery to the ridge axis that leads to some of the melt being trapped and pooled in lenses within the MTZ (Figure 9) [*Aghaei et al.*, 2014], providing potential reservoirs of melt to supply crustal OAMLs.

Detailed reflection mapping of the MTZ character in the study area shows that the two large midcrustal OAMLs are found within regions of dominantly diffusive Moho reflection response, as are the majority of the lower crustal OAMLs [*Aghaei*, 2013]. However, the regions with a thick MTZ located from 9°37.5' to 9°40'N and from 9°50' to 9°57'N cover an area that is much larger than the area covered by the OAMLs. Moreover, a thick MTZ is imaged on the Pacific plate in regions where no midcrustal OAMLs are imaged [*Aghaei et al.*, 2014]. These observations suggest that the presence of a subcrustal melt reservoir in the form of MTZ magma lenses may not be sufficient to form and sustain the midcrustal OAMLs and that local thermal heterogeneity may be required to facilitate melt migration from the uppermost mantle to the midcrust (Figure 9). Enriched MORBs, indicating the presence of local mantle heterogeneities, have been sampled on the EPR 9°–10°N ridge flanks at distances >0.5 km away from the ridge axis [*Perfit et al.*, 1994; *Smith et al.*, 2001;

*Sims et al., 2003; Waters et al., 2011*], and their off-axis origin is supported by the OAMLs imaged using seismic data [*Canales et al., 2012; Aghaei, 2013; Han et al., 2014*]. The presence of local thermal anomalies has also been predicted from the thermochemical modeling of *Katz and Weatherley [2012]* for melt extraction at mid-ocean ridges. These models suggest that magmatic segregation from a chemically heterogeneous mantle results in melt pooling and crystallization at the base of the lithosphere. These melt pools may supply magma to the OAMLs through high-porosity, high-permeability channels or dikes as is inferred for the axial zone.

Without new detailed geochemical studies, it is not possible to distinguish which of the two discussed most plausible options for the melt-source reservoir has given rise to the investigated midcrustal OAMLs. However, there is strong evidence in support of vertical or near vertical melt migration as opposed to lateral transport from the axial zone. Little or no Moho reflection response is observed directly below the midcrustal OAMLs, and at some places around them, suggesting that the MTZ is overprinted, most likely because of the upward melt delivery from the uppermost mantle to the crust. Seismic waves recorded on ocean bottom seismometers and propagating through the lower crust below the northern midcrustal OAMLs show strongly attenuated amplitudes due to interstitial melt [*Canales et al., 2012*]. No such attenuation of seismic waves is observed outside the regions covered by this OAML and within the area covered by the northern 3-D seismic volume. Although there are no seismic attenuation data available for the crust below the southern midcrustal OAML, the optimal migration velocity between this large midcrustal and a smaller underlying lower crustal OAML (Figure 3a) is lower than expected for normal oceanic layer 3 and similar to that in the same interval for the northern midcrustal OAML [*Aghaei, 2013*].

## 7. Conclusions

We use 3-D MCS data to form partial angle *P* wave stacks and apply the AVA crossplotting technique to assess melt content and melt distribution within two large midcrustal OAMLs found along the northern EPR from 9°37.5'N to 9°57'N. This is the first magma melt content study using high-resolution 3-D MCS data and the first such investigation targeting OAMLs. The northern OAML is divided into study Zones A and B, while the southern OAML has one study Zone C. For AVA crossplotting, Zones B and C are both subdivided into three analysis windows. Each of the seven analyses windows covers an area of ~1 km<sup>2</sup>.

The obtained results indicate that the investigated OAMLs are in a partially molten state. The spatial transitions in trace envelope of the *P* wave partial angle stacks, and the difference between them, indicate that the melt content is on average likely highest in Zone C and lowest in Zone A, and that its distribution is most uniform in Zone C and least uniform in Zone A. The results of AVA crossplotting show that the two investigated OAMLs on average contain a smaller amount of melt (<20%) than the AML. The section of the northern OAML covered by the single analysis window of Zone A, which is farther from the ridge axis and deeper than any other analysis window, appears to have the least melt. Parts of the OAMLs in Zones B and C covered by analysis windows 1 and located closest to the ridge axis appear to, on average, have more melt than the more distant windows 3. The highest combined melt concentration is interpreted for windows 2 of Zones B and C found in the middle sections of the OAMLs. The reflection volume shows domal shape in the central area of the OAMLs, which likely allows for greater melt pooling.

The apparent low melt content of the investigated midcrustal OAMLs may be indicative of one or a combination of the following: (1) melt lost due to recent off-axis eruptions preceding our 2008 survey, (2) melt drainage to the AML, and (3) limited mantle melt supply. The first possibility is unlikely because, although off-axis eruptions sourced from the OAML have built local volcanic constructs directly above the investigated OAMLs [e.g., *Han et al., 2014*], recent dives did not reveal fresh unsedimented volcanics (S. M. White, personal communication, 2016). While no connectivity is imaged between the midcrustal OAML and the AML, some melt migration from the midcrustal OAMLs toward the AML is supported by (a) the spatial extent and geometry of the midcrustal OAMLs and the AML, (b) the greater estimated melt content for the OAML sections toward the ridge axis in comparison to sections farthest away, and (c) the relatively lower melt content of the northern OAML near axis area found east of the axial region that erupted in 2005–2006.

The likely dominant cause for the melt-poor OAMLs is limited melt supply from the underlying mantle source reservoir. The lack of significant total crust or layer 2A thickness anomalies associated with these features [*Han et al., 2014*] indicates the time-averaged flux of melt to the OAML could be only a fraction of that

focused to the axial zone. Limited mantle melt supply, combined with some melt migration to the AML, is expected to result in lower rates of melt replenishment, OAML eruption recurrence rates and volumes that are lower than for the AML, and low OAML melt content even when replete, in part because of partial crystallization due to a longer cooling period. Some fraction of the OAMLs could also reflect single intrusion events that rapidly cool and solidify after off-axis intrusion into a relative cool host rock.

A direct comparison between the estimated OAML melt content from this study and the estimates for the AML melt content presented in earlier studies is not possible. This is because the computations done in this work were carried out in 3-D and are representative of the average melt content of the OAMLs, which contrasts with the 1-D and 2-D studies carried out so far that resulted in estimates of the melt content only for the central, most melt-rich points or profiles across the targeted AMLs. Nevertheless, the first-order observations of lower melt content of the investigated midcrustal OAMLs in comparison to the AML, and the nature of its distribution within these magma lenses, are robust. Further understanding of the AML and OAML melt content and the relationship between these two types of magma lenses will require collection and analysis of complementary geochemical and geophysical data sets.

#### Acknowledgments

This research was supported by NSERC Discovery, CRC, and CFI grants to M.R.N. and National Science Foundation grants OCE0327872 to S.M.C., OCE327885 to J.P.C., and OCE0624401 to M.R.N. Data analysis was carried out using Paradigm Geophysical Ltd. The data and corresponding metafiles used in this work are freely available for download from the Marine Geoscience Data System, which is a part of the Interdisciplinary Earth Data Alliance funded by the U.S. National Science Foundation. O.A. analyzed the data guided by M.R.N. and discussions with all authors. M.R.N. wrote the manuscript with input from all authors.

#### References

- Aghaei, O. (2013), The East Pacific rise crustal thickness, Moho transition zone character and off-axis magma lens melt content from 9°37.5'N TO 9°57'N: Results from three-dimensional multichannel seismic data analysis, PhD thesis.
- Aghaei, O., M. R. Nedimović, H. Carton, S. M. Carbotte, J. P. Canales, and J. C. Mutter (2014), Crustal thickness and Moho character of the fast-spreading East Pacific Rise from 9°42'N to 9°57'N from poststack-migrated 3D MCS data, *Geochem. Geophys. Geosyst.*, *15*, 634–657, doi:10.1002/2013GC005069.
- Aki, K. I., and P. G. Richards (1980), *Quantitative Seismology, Theory and Methods*, vol. 1, 557 pp., W. H. Freeman and Co., New York.
- Anderson, D. L., and H. Spetzler (1970), Partial melting and the low-velocity zone, *Phys. Earth Planet. Inter.*, *4*(1), 62–64, doi:10.1016/0031-9201(70)90030-0.
- Bacon, M., R. Simm, and T. Redshaw (2007), *3-D Seismic Interpretation*, 212 pp., Cambridge Univ. Press, Cambridge, U. K.
- Brocher, T. A., J. A. Karson, and J. A. Collins (1985), Seismic stratigraphy of the oceanic Moho based on ophiolite models, *Geology*, *13*, 62–65, doi:10.1130/0091-7613(1985)13<62:SSOTOM>2.0.CO;2.
- Canales, J. P., S. C. Singh, R. S. Detrick, S. M. Carbotte, A. J. Harding, G. M. Kent, J. B. Diebold, J. Babcock, and M. R. Nedimović (2006), Seismic evidence for variations in axial magma chamber properties along the southern Juan de Fuca ridge, *Earth Planet. Sci. Lett.*, *246*, 353–366.
- Canales, J. P., M. R. Nedimović, G. M. Kent, S. M. Carbotte, and R. S. Detrick (2009), Seismic reflection images of a near-axis melt sill within the lower crust at the Juan de Fuca ridge, *Nature*, *460*, 89–93, doi:10.1038/nature08095.
- Canales, J. P., H. Carton, S. M. Carbotte, J. C. Mutter, M. R. Nedimović, M. Xu, O. Aghaei, M. Marjanović, and K. Newman (2012), Network of off-axis melt bodies at the East Pacific Rise, *Nat. Geosci.*, *5*, 279–283, doi:10.1038/ngeo1377.
- Canales, J. P., R. A. Dunn, G. Ito, R. S. Detrick, and V. Sallarés (2014), Effect of variations in magma supply on the crustal structure of mid-ocean ridges: Insights from the western Galapagos spreading center, in *The Galapagos: A Natural Laboratory for the Earth Sciences*, edited by N. d'Ozouville et al., pp. 363–391, John Wiley, Hoboken, N. J.
- Carbotte, S. M., and K. Macdonald (1992), East Pacific Rise 8°–10°30'N: Evolution of ridge segments and discontinuities from SeaMARC II and three-dimensional magnetic studies, *J. Geophys. Res.*, *97*, 6959–6982, doi:10.1029/91JB03065.
- Carbotte, S. M., J. C. Mutter, and L. Q. Xu (1997), Contribution of volcanism and tectonism to axial and flank morphology of the southern East Pacific Rise, 17° 10'–17° 40' S, from a study of layer 2A geometry, *J. Geophys. Res.*, *102*, 10,165–10,184, doi:10.1029/96JB03910.
- Carbotte, S. M., M. Marjanović, H. Carton, J. C. Mutter, J. P. Canales, M. R. Nedimović, S. Han, and M. R. Perfit (2013), Fine-scale segmentation of the crustal magma reservoir beneath the East Pacific Rise, *Nat. Geosci.*, *6*, 866–870, doi:10.1038/ngeo1933.
- Caricchi, L., L. Burlini, and P. Ulmer (2009), Propagation of P and S waves in magmas with different crystal contents: Insights into the crystallinity of magmatic reservoirs, *J. Volcanol. Geotherm. Res.*, *178*, 740–750.
- Carlson, R. L. (2001), Rock and Earth's crust, in *Handbook of Elastic Properties of Solids, Liquids, and Gases, Elastic Prop. Solids: Biol. Org. Mater., Earth Mar. Sci.*, vol. 3, pp. 377–461, edited by M. Levy et al., Academic Press, New York.
- Castagna, J. P., and S. W. Smith (1994), Comparison of AVO indicators: A modeling study, *Geophysics*, *59*, 1849–1855, doi:10.1190/1.1443572.
- Castagna, J. P., and H. W. Swan (1997), Principles of AVO crossplotting, *Leading Edge*, *16*, 337–342, doi:10.1190/1.1437626.
- Castagna, J. P., M. L. Batzle, and R. L. Eastwood (1985), Relationships between compressional-wave and shear-wave velocities in clastic silicate rocks, *Geophysics*, *50*, 571–581, doi:10.1190/1.1441933.
- Castagna, J. P., H. W. Swan, and D. J. Foster (1998), Framework for AVO gradient and intercept interpretation, *Geophysics*, *63*, 948–956, doi:10.1190/1.1444406.
- Choo, J., J. Downton, and J. Dewar (2004), Lift: A new and practical approach to noise and multiple attenuation, *First Break*, *22*, 39–44, doi:10.3997/1365-2397.2004009.
- Collier, J. S., and S. C. Singh (1997), Detailed structure of the top of the melt body beneath the East Pacific Rise at 9°40'N from waveform inversion of seismic reflection data, *J. Geophys. Res.*, *102*, 20,287–20,304, doi:10.1029/97JB01514.
- Collier, J. S., and S. C. Singh (1998), A seismic inversion study of the axial magma chamber reflector beneath the East Pacific Rise near 10°N, in *Modern Ocean Floor Processes and the Geological Record*, edited by R. A. Mills and K. Harrison, *Geol. Soc. Spec. Publ.*, 17–28.
- Collins, J. A., T. M. Brocher, and J. A. Karson (1986), Two-dimensional seismic reflection modeling of the inferred crust-mantle transition in the Bay of Islands ophiolite, *J. Geophys. Res.*, *91*, 12,520–12,538, doi:10.1029/JB091iB12p12520.
- Crawford, W. C., and S. C. Webb (2002), Variations in the distribution of magma in the lower crust and at the Moho beneath the East Pacific Rise at 9°–10°N, *Earth Planet. Sci. Lett.*, *203*, 117–130, doi:10.1016/S0012-821X(02)00831-2.
- Detrick, R. S., P. Buhl, E. Vera, J. Mutter, J. Orcutt, J. Madsen, and T. Brocher (1987), Multi-channel seismic imaging of a crustal magma chamber along the East Pacific Rise, *Nature*, *326*, 35–41, doi:10.1038/326035a0.

- Dunn, R. A., D. R. Toomey, and S. C. Solomon (2000), Three-dimensional seismic structure and physical properties of the crust and shallow mantle beneath the East Pacific Rise at 9°30'N, *J. Geophys. Res.*, *105*, 23,537–23,555, doi:10.1029/2000JB900210.
- Durant, D. T., and D. R. Toomey (2009), Evidence and implications of crustal magmatism on the flanks of the East Pacific Rise, *Earth Planet. Sci. Lett.*, *287*, 130–136, doi:10.1016/j.epsl.2009.08.003.
- Forsyth, D. W. (1992), Geophysical constraints on mantle flow and melt generation beneath mid-ocean ridges, in *Mantle Flow and Melt Generation at Mid-Ocean Ridges*, *Geophys. Monogr. Ser.*, vol. 71, edited by J. P. Morgan, D. K. Blackman, and J. M. Sinton, pp. 1–65.
- Foster, D. J., R. G. Keys, and F. D. Lane (2010), Interpretation of AVO anomalies, *Geophysics*, *75*, 75A3–75A13, doi:10.1190/1.3467825.
- Gardner, G. H. F., L. W. Gardner, and A. R. Gregory (1974), Formation velocity and density—The diagnostic basics for stratigraphic traps, *Geophysics*, *39*, 770–780.
- Garmany, J. (1989), Accumulations of melt at the base of young oceanic-crust, *Nature*, *340*, 628–632, doi:10.1038/340628a0.
- Goldstein, S. J., M. R. Perfit, R. Batiza, D. J. Fornari, and M. T. Murrell (1994), Off-axis volcanism at the East Pacific Rise detected by uranium-series dating of basalts, *Nature*, *367*, 157–159, doi:10.1038/367157a0.
- Goss, A. R., M. R. Perfit, W. I. Ridley, K. H. Rubin, G. D. Kamenov, S. A. Soule, A. T. Fundis, and D. J. Fornari (2010), Geochemistry of lavas from the 2005–2006 eruption at the East Pacific Rise, 9°46'N–9°56'N: Implications for ridge crest plumbing and decadal changes in magma chamber compositions, *Geochem. Geophys. Geosyst.*, *11*, Q05T09, doi:10.1029/2009GC002977.
- Han, S., S. M. Carbotte, H. Carton, J. C. Mutter, O. Aghaei, M. R. Nedimović, and J. P. Canales (2014), Architecture of off-axis magma bodies at EPR 9°37'–40'N and implications for oceanic crustal accretion, *Earth Planet. Sci. Lett.*, *390*, 31–44, doi:10.1016/j.epsl.2013.12.040.
- Harding, A. J., G. M. Kent, and J. A. Orcutt (1993), A multichannel seismic investigation of upper crustal structure at 9°N on the East Pacific Rise: Implications for crustal accretion, *J. Geophys. Res.*, *98*, 13,925–13,944, doi:10.1029/93JB00886.
- Hashin, Z., and S. Shtrikman (1963), A variational approach to the theory of the elastic behaviour of multiphase materials, *J. Mech. Phys. Solids*, *11*, 127–140, doi:10.1016/0022-5096(63)90060-7.
- Haymon, R. M., et al. (1993), Volcanic eruption of the mid-ocean ridge along the East Pacific Rise crest at 9°45'–52'N: Direct submersible observations of seafloor phenomena associated with an eruption event in April, 1991, *Earth Planet. Sci. Lett.*, *119*, 85–101, doi:10.1016/0012-821X(93)90008-W.
- Herron, T. J., W. J. Ludwig, P. L. Stoffa, T. K. Kan, and P. Buhl (1978), Structure of the East Pacific Rise from multichannel seismic reflection data, *J. Geophys. Res.*, *83*, 798–804, doi:10.1029/JB083iB02p00798.
- Herron, T. J., P. L. Stoffa, and P. Buhl (1980), Magma chamber and mantle reflections—East Pacific Rise, *Geophys. Res. Lett.*, *7*, 989–992, doi:10.1029/GL007i011p00989.
- Hussenöeder, S. A., J. A. Collins, G. M. Kent, R. S. Detrick, and the TERA Group (1996), Seismic analysis of the axial magma chamber reflector along the southern East Pacific Rise from conventional reflection profiling, *J. Geophys. Res.*, *101*, 22,087–22,105, doi:10.1029/96JB01907.
- Iturrino, G. J., N. I. Christensen, S. Kirby, and M. H. Salisbury (1991), Seismic velocities and elastic properties of oceanic gabbroic rocks from hole 735B, in *Proceedings of the Ocean Drilling Program, Sci. Results*, vol. 118, edited by R. P. Von Herzen et al., pp. 227–244, Ocean Drilling Program, College Station, Tex.
- Katz, R. F., and S. M. Weatherley (2012), Consequences of mantle heterogeneity for melt extraction at mid-ocean ridges, *Earth Planet. Sci. Lett.*, *335–336*, 226–237, doi:10.1016/j.epsl.2012.04.042.
- Kent, G. M., A. J. Harding, and J. A. Orcutt (1993), Distribution of magma beneath the East Pacific Rise between the Clipperton transform and the 9°17'N deval from forward modeling of common depth point data, *J. Geophys. Res.*, *98*, 13,945–13,969, doi:10.1029/93JB00705.
- Macdonald, K. C. (1998), Linkages between faulting, volcanism, hydrothermal activity and segmentation on fast spreading centers, in *Faulting and Magmatism at Mid-Ocean Ridges*, edited by W. R. Buck et al., pp. 27–58, AGU, Washington, D. C.
- Marjanović, M., S. M. Carbotte, H. Carton, M. R. Nedimović, J. C. Mutter, and J. P. Canales (2014), A multi-sill magma plumbing system beneath the axis of the East Pacific Rise, *Nat. Geosci.*, *7*, 825–829, doi:10.1038/NNGEO2272.
- Marjanović, M., H. Carton, S. M. Carbotte, M. R. Nedimović, J. C. Mutter, and J. P. Canales (2015), Distribution of melt along the East Pacific Rise from 9°30' to 10°N from an amplitude variation with angle of incidence (AVA) technique, *Geophys. J. Int.*, *203*, 1–21, doi:10.1093/gji/ggv251.
- Mavko, G. M. (1980), Velocity and attenuation in partially molten rocks, *J. Geophys. Res.*, *85*, 5173–5189, doi:10.1029/JB085iB10p05173.
- Murase, T., and A. R. McBirney (1973), Properties of some common igneous rocks and their melts at high temperatures, *Geol. Soc. Am. Bull.*, *84*, 3563–3592, doi:10.1130/0016-7606(1973)84<3563:POSCIR>2.0.CO;2.
- Mutter, J. C., S. M. Carbotte, M. R. Nedimović, J. P. Canales, and H. Carton (2009), Seismic imaging in three dimensions on the East Pacific Rise, *Eos. Trans. AGU*, *90*, 374–375, doi:10.1029/2009EO420002.
- Nedimović, M. R., S. M. Carbotte, A. J. Harding, R. S. Detrick, J. P. Canales, J. B. Diebold, G. M. Kent, M. Tischer, and J. M. Babcock (2005), Frozen magma lenses below the oceanic crust, *Nature*, *436*, 1149–1152, doi:10.1038/nature03944.
- Peles, O., D. Kosloff, Z. Koren, and M. Tygel (2001), A practical approach to true amplitude migration, *J. Seism. Explor.*, *10*, 183–203.
- Perfit, M. R., and W. W. Chadwick (1998), Magmatism at mid-ocean ridges: Constraints from volcanological and geochemical investigations, in *Faulting and Magmatism at Mid-Ocean Ridges*, edited by W. R. Buck et al., pp. 59–115, AGU, Washington, D. C., doi:10.1029/GM106p0059.
- Perfit, M. R., D. J. Fornari, M. C. Smith, J. F. Bender, C. H. Langmuir, and R. M. Haymon (1994), Small-scale spatial and temporal variations in mid-ocean ridge crest magmatic processes, *Geology*, *22*, 375–379, doi:10.1130/0091-7613(1994)022<0375:SSSATV>2.3.CO;2.
- Ross, C. (2000), Effective AVO crossplot modeling a tutorial, *Geophysics*, *65*, 700–711, doi:10.1190/1.1444769.
- Rutherford, S. R., and R. H. Williams (1989), Amplitude-versus-offset variations in gas sands, *Geophysics*, *54*, 680–688, doi:10.1190/1.1442696.
- Singh, S. C., et al. (2006), Seismic reflection images of the Moho underlying melt sills at the East Pacific Rise, *Nature*, *442*, 287–290.
- Shuey, R. T. (1985), A simplification of the Zeppritz equations, *Geophysics*, *50*, 609–614, doi:10.1190/1.1441936.
- Sims, K. E., et al. (2003), Aberrant youth: Chemical and isotopic constraints on the origin of off-axis lavas from the East Pacific Rise, 9°–10°N, *Geochem. Geophys. Geosyst.*, *4*(10), 8621, doi:10.1029/2002GC000443.
- Singh, S. C., G. M. Kent, J. S. Collier, A. J. Harding, and J. A. Orcutt (1998), Melt to mush variations in crustal magma properties along the ridge crest at the southern East Pacific Rise, *Nature*, *394*, 874–878, doi:10.1038/29740.
- Smith, M. C., M. R. Perfit, D. J. Fornari, W. I. Ridley, M. E. Edwards, G. Kurras, and K. L. Von Damm (2001), Magmatic processes and segmentation at a fast spreading mid-ocean ridge: Detailed investigation of an axial discontinuity on the East Pacific Rise crest at 9°37'N, *Geochem. Geophys. Geosyst.*, *2*, 1040, doi:10.1029/2000GC000134.
- Soule, S. A., D. J. Fornari, M. R. Perfit, and K. Rubin (2007), New insights into mid-ocean ridge volcanic processes from the 2005–2006 eruption of the East Pacific Rise, 9°46'N–9°56'N, *Geology*, *35*, 1079–1082, doi:10.1130/G23924A.1.
- Soule, S. A., J. Escartin, and D. J. Fornari (2009), A record of eruption and intrusion at a fast spreading ridge axis: Axial summit trough of the East Pacific Rise 9–10°N, *Geochem. Geophys. Geosyst.*, *10*, Q10T07, doi:10.1029/2008GC002354.
- Taner, M. T., F. Koehler, and R. E. Sheriff (1979), Complex seismic trace analysis, *Geophysics*, *44*, 1041–1063, doi:10.1190/1.1440994.

- Tolstoy, M., et al. (2006), A sea-floor spreading event captured by seismometers, *Science*, *314*, 1920–1922, doi:10.1126/science.1133950.
- Toomey, D. R., D. Jouselin, R. A. Dunn, W. S. D. Wilcock, and R. S. Detrick (2007), Skew of mantle upwelling beneath the East Pacific Rise governs segmentation, *Nature*, *446*, 409–414, doi:10.1038/nature05679.
- Vera, E. E., J. C. Mutter, P. Buhl, J. A. Orcutt, A. J. Harding, M. E. Kappus, R. S. Detrick, and T. M. Brocher (1990), The structure of 0- to 0.2-m.y.-old oceanic crust at 9°N on the East Pacific Rise from expanded spread profiles, *J. Geophys. Res.*, *95*, 15,529–15,556, doi:10.1029/JB095iB10p15529.
- Waters, C. L., K. W. W. Sims, M. R. Perfit, J. Blichert-Toft, and J. Blusztajn (2011), Perspective on the genesis of E-MORB from chemical and isotopic heterogeneity at 9–10°N East Pacific Rise, *J. Petrol.*, *52*, 565–602, doi:10.1093/ptrology/egq091.
- Xu, M., J. P. Canales, S. M. Carbotte, H. Carton, M. R. Nedimović, and J. C. Mutter (2014), Variations in axial magma lens properties along the East Pacific Rise (9°30'–10°00'N) from swath 3D seismic imaging and 1-D waveform inversion, *J. Geophys. Res. Solid Earth*, *119*, 2721–2744, doi:10.1002/2013JB010730.
- Yilmaz, O. (2001), *Seismic Data Analysis: Processing, Inversion, and Interpretation of Seismic Data*, Invest. Geophys., vol. 1, 1000 pp., edited by M. R. Cooper, Soc. of Explor. Geophys.
- Zoeppritz, K. (1919), Erdbebenwellen VIII B, on the reflection and propagation of seismic waves, *Gottinger Nachr.*, *1*, 66–84.